TAMPEREEN TEKNILLINEN YLIOPISTO
TAMPERE UNIVERSITY OF TECHNOLOGY

TAPIO PELTOMAA

PARAMETRIZATION OF FORCE FIELDS FOR MOLECULAR DYNAMICS SIMULATIONS OF ORGANIC SOLAR CELL POLYMERS

Master of Science thesis

Examiners: Docent, university lecturer Terttu Hukka and M.Sc. (Tech.), doctoral student Tuuva Kastinen.
Examiners and topic approved by the Faculty Council of the Faculty of Natural Sciences on 29th March 2017

ABSTRACT

TAPIO PELTOMAA: Parametrization of Force Fields for Molecular Dynamics Simulations of Organic Solar Cell Polymers
Tampere University of Technology
Master of Science thesis, 68 pages, 5 Appendix pages
July 2017
Master's Degree Programme in Science and Engineering
Major: Chemistry
Examiner: Docent, university lecturer Terttu Hukka and M.Sc. (Tech.), doctoral student Tuuva Kastinen
Keywords: Force field parametrization, molecular dynamics, donor–acceptor copolymer, polymer solar cells

With the flexibility of the material, cheaper production costs and the use of organic materials, polymer solar cells (PSC) present an alternative to silicon-based solar cells. The working principle of PSCs is dependent on the morphology of an active layer, which absorbs photons, generates charges and separates them to electrodes generating current. The active layer consists of electron donor (eD) and electron acceptor (eA) phases, with the eD often being a conjugated donor–acceptor copolymer and eA a fullerene derivative. Research on the development of PSCs continues, but not everything about how different factors affect the morphology of the active layer is known.

To gain a better understanding of the relationship between the morphology and the performance of a PSC, a molecular level knowledge of the active layer is required. This can be gained computationally by simulating models representing real systems, with methods such as molecular dynamics (MD). However, for the MD simulations to describe the studied molecule accurately, it requires a force field that contains exact information about the atoms and their interactions with each other. The goal of this thesis was to parametrize a OPLS-AA -based force field for a PBDT-TPD polymer which is often used as the eD material in PSCs, and test its performance by simulating it in a solvent system and in both crystalline and amorphous phases.

Presented here is the final force field that contains all the required parameters for the studied polymer and is designed for simulation with the GROMACS software. The simulations conducted here prove that it produces results that are comparable to other computational and experimental studies. In the future, the force field can be used in larger scale computational studies of the active layer morphology.

TIIVISTELMÄ

TAPIO PELTOMAA: Voimakentän parametrisointi orgaanisten aurinkokennopolymeerien molekyylidynamiikkasimulaatioihin.
Tampereen teknillinen yliopisto
Diplomityö, 68 sivua, 5 liitesivua
Heinäkuu 2017
Teknis-luonnontieteellinen tutkinto-ohjelma
Pääaine: Kemia
Tarkastajat: Dosentti, yliopistonlehtori Terttu Hukka ja DI, tohtorikoulutettava Tuuva Kastinen
Avainsanat: Voimakentän parametrisointi, molekyylidynamiikka, donori–akseptori kopolymeeri, polymeeriaurinkokennot

Materiaalin joustavuuden, halvempien tuotantokustannuksien ja orgaanisten materiaalien käytön vuoksi polymeeriaurinkokennot (PSC) tarjoavat vaihtoehdon piipohjaisille aurinkokennoille. PSC:n aktiivinen kerros absorboi fotoneja, tuottaa varauksia ja erottaa ne elektrodeille luoden sähkövirtaa, ja PSC:n toimintaperiaate on riippuvainen sen morfologiasta. Aktiivinen kerros koostuu kahdesta faasista: elektronidonorista (eD) ja elektroniakseptorista (eA), joissa eD:na toimii usein konjugoitunut donori–akseptori kopolymeeri ja eA:na fullereenijohdannainen. PSC:ien kehittämiseksi tehdään jatkuvaa tutkimusta, mutta kaikkea eri tekijöiden vaikutuksesta aktiivisen kerroksen morfologiaan ei vielä tiedetä.

Paremman ymmärryksen saavuttamiseksi morfologian ja PSC:n ominaisuuksien välisestä suhteesta tarvitaan molekyylitason tietämystä aktiivisesta kerroksesta. Tämä voidaan saavuttaa laskennallisesti simuloimalla todellisia systeemejä kuvaavia malleja metodeilla kuten molekyylidynamiikalla (MD). Jotta MD simulaatiot voivat kuvata tutkittavaa molekyyliä tarkasti, tarvitaan voimakenttä, joka sisältää täsmällistä informaatiota atomeista ja niiden välisistä vuorovaikutuksista. Tämän diplomityön tavoitteena oli parametrisoida tällainen OPLS-AA tyyppinen voimakenttä PBDT-TPD polymeerille, jota käytetään usein PSC:ssa eD-materiaalina, ja testata sen toimintaa simuloimalla liuosysteemiä ja sekä kiteistä että amorfista morfologiaa.

Työssä esitellään GROMACS -ohjelmistolla simulaatioihin suunniteltu valmis voimakenttä, joka sisältää kaikki tarvittavat parametrit tutkittavalle polymeerille. Työn simulaatiot osoittavat, että voimakenttä tuottaa muihin laskennallisiin ja kokeellisiin tutkimuksiin verrattavia tuloksia. Jatkossa voimakenttää voidaan käyttää kooltaan suuremman aktiivisen kerroksen morfologian laskennallisissa tutkimuksissa.

PREFACE

The work with this Master of Science thesis was carried out between January and June 2017 at the Laboratory of Chemistry and Bioengineering at Tampere University of Technology. The goal of the thesis was to outline the process of parametrizing a force field that could be used for simulating and studying an organic solar cell polymer by molecular dynamics. Resources for these computational methods were provided by Centre for Scientific Computing (CSC) – IT center for science.

I would like to thank Docent Terttu Hukka for providing me an opportunity to do this thesis under her guidance. Also thanks for M.Sc.Tech Tuuva Kastinen for teaching me the force field parametrization process and providing helpful advice whenever needed.

I also express my gratitude to my parents for all their support and encouragement. Also thanks to all my friends for their priceless company throughout all my years at the university and for providing some helpful peer support. Finally, extra thanks to Adam for always believing in me and supporting me during this whole process.

Tampere, 31st July 2017

Tapio Peltomaa

TABLE OF CONTENTS

LIST OF FIGURES

LIST OF TABLES

LIST OF ABBREVIATIONS AND SYMBOLS

A	Acceptor moiety in a donor–acceptor copolymer
AO	Atomic orbital
BDT	benzo[1,2-*b*:4,5-*b*']dithiophene, polymer backbone donor residue
BHJ	Bulk heterojunction
CC license	Creative Commons license
CGTO	Contracted Gaussian-type orbital
ChelpG	Charges from the Electrostatic Potential on a Grid
CRU	Constitutional repeating unit
CSC	Center for Scientific Computing
D	Donor moiety in a donor–acceptor copolymer
DFT	Density functional theory
eA	Electron acceptor
eD	Electron donor
EHX	2-ethylhexyl side chain residue
EM	Energy minimization
GAFF	General Amber Force Field
GGA	Generalized gradient approximation
GROMACS	GROMACS molecular dynamics software package
GTO	Gaussian-type orbital
HEP	Heptyl side chain residue
HF	Hartree–Fock
HOMO	Highest occupied molecular orbital
ITO	Indium tin oxide
LAMMPS	LAMMPS molecular dynamics software package
LDA	Local density approximation
LRC	Long-range corrected
LUMO	Lowest unoccupied molecular orbital
MD	Molecular dynamics
MK	Merz–Singh–Kollman
MTTK	Martyna–Tuckerman–Tobias–Klein barostat
NAMD	NAMD molecular dynamics software package
NPT	Isothermal–isobaric ensemble, N, p and T are constant
NVT	Canonical ensemble, N, V and T are constant
OPLS-AA	Optimized Potentials for Liquid Simulations - All Atom
OSC	Organic solar cell

PBC	Periodic boundary conditions
PBDT-TPD	Poly(benzo[1,2-*b*:4,5-*b*']dithiophene-thieno[3,4-*c*]pyrrole-4,6-dione)
PCE	Power conversion efficiency
PET	Polyethylene terephthalate
P3M-AD	Particle-particle particle-mesh algorithm
PSC	Polymer solar cell
Q-CHEM	Q-CHEM *ab initio* quantum chemistry software package
QM	Quantum mechanics
RB	Ryckaert–Bellemans
RESP	Restricted electrostatic potential
TD-DFT	Time-dependent density functional theory
TINKER	TINKER molecular dynamics software package
TPD	thieno[3,4-*c*]pyrrole-4,6-dione, polymer backbone acceptor residue
VMD	Visual Molecular Dynamics

b_{ij}	bond length between atoms i and j
b_{ij}^0	reference bond length between atoms i and j
C_0–C_5	Ryckaert–Bellemans type dihedral coefficients
c	speed of light
d_n	maximum displacement
E_0	ground state energy
E_e	electronic energy
E_g	band gap
E_n	nuclear repulsion term
E_{photon}	energy of a photon
E_{TOT}	total energy
E_{xc}	electron-electron exchange-correlation energy functional
ΔE_ψ	potential energy difference between DFT and EM methods
$E_{\psi,0}$	potential energy with the lowest value
$E_{\psi,i}$	potential energy value of frozen dihedral angle structure i
$E_{\psi,DFT}$	potential energy value relative to the lowest energy with DFT
$E_{\psi,EM}$	potential energy value with EM
$\mathbf{F}$	force vector
$\max(\lvert\mathbf{F}_n\rvert)$	largest absolute value of the force components
F_1–F_4	Fourier type dihedral coefficients
F_{HK}	Hohenberg–Kohn functional
$\hat{H}$	Hamiltonian operator
$\hat{H}_e$	electronic Hamiltonian operator

h	Planck constant
i	index
j	index
k	index
k_B	Boltzmann constant
k_{ij}^{b}	bond force constant between atoms i and j
k_{ijk}^{θ}	angular force constant between atoms i, j and k
k_{ijkl}^{ξ}	improper dihedral force constant between atoms i, j, k and l
l	index
m	mass
N	number of particles
P	probability
p	pressure
q	partial charge
$\mathbf{R}$	a set of nuclear coordinates
$\mathbf{r}$	location vector
r_{ij}	distance between atoms i and j
$\mathbf{S}$	sum of squared deviations
T	absolute temperature
t	time
Δt	time step
$\hat{T}_e$	kinetic energy of the electrons
T_e	kinetic energy of the electrons in ground state
$\hat{T}_n$	kinetic energy of the nuclei
U_{angles}	potential of angle bending
U_{bonded}	potential of bonded interactions
U_{bonds}	potential of bond stretching
$U_{Coulomb}$	potential of Coulomb interaction
$U_{dihedrals}$	potential of dihedrals
$U_{impropers}$	potential of improper dihedral out of plane bending
$U_{Lennard-Jones}$	potential of Lennard–Jones interaction
$U_{propers}$	potential of proper dihedral angle torsion
U_{RB}	potential of Ryckaert–Bellemans type proper dihedral angle torsion
U_{TOT}	total potential
V	volume
$\mathbf{v}$	velocity vector
v	velocity
$\hat{V}_{ee}$	repulsive electron-electron potential
V_{ee}	repulsive electron-electron potential in ground state

$\hat{V}_{en}$	attractive electron-nucleus potential
V_{en}	attractive electron-nucleus potential in ground state
$\hat{V}_{nn}$	repulsive nucleus-nucleus potential
$\mathbf{x}$	a set of electronic coordinates
ϵ	Lennard–Jones parameter
ϵ_r	relative permittivity
ϵ_0	vacuum permittivity
θ_{ijk}	angle between atoms i, j and k
θ^0_{ijk}	reference angle between atoms i, j and k
λ	wavelength
ν	frequency
ξ_{ijkl}	improper dihedral angle between atoms i, j, k and l
ξ^0_{ijkl}	reference improper dihedral angle between atoms i, j, k and l
$\boldsymbol{\rho}$	electron density
σ	Lennard–Jones parameter
Φ_f	work function
ϕ	proper dihedral angle for Fourier type dihedral
ψ	proper dihedral angle for Ryckaert–Bellemans type dihedral
Ψ	wave function
Ψ_e	electronic wave function
ω	range separation parameter

1. INTRODUCTION

The energy consumption of the world is rising constantly, and so are the needs for cleaner and renewable methods for producing energy. With their lower production costs and the use of organic materials, polymer solar cells (PSC) present a new interesting alternative compared to the silicon-based solar cells of the earlier generations [1]. To achieve best performance in PSCs, the optimal morphology of the active layer is extremely important [2]. This active layer absorbs photons, generates charges and separates them to electrodes, which creates an electric current in the device [3]. The active layer contains electron donor (eD) and electron acceptor (eA) phases, and in PSCs the eD material is usually a conjugated donor–acceptor copolymer, and the eA material a fullerene derivative [4]. For the best performance, both these phases must form a continuous network, their distance from each other must be optimal and the surface area between must be as large as possible, as this enhances the charge transfer between the phases [2].

However, not everything about how different factors such as different polymer backbones, side chains or substituents affect the morphology of the active layer is yet understood. Knowledge about the structure–property relationship between the active layer morphology and the performance of the solar cells is the key for achieving even better performances in these devices. This requires a molecular level understanding on how different atoms interact with each other and how these interactions affect the morphology. The way of gaining such knowledge is through computational methods, in which accurate models of real systems can be built, and these models can be used in simulations giving insight to behaviour of these real systems. [5]

One of the many possible computational methods available for simulations is molecular dynamics (MD), which relies on classical mechanics such as Newton's laws for describing the interactions and movement of atoms in the system as a function of time [6, p. 16]. At the core of the MD method is a force field, which contains all the information about the properties of the atoms in the system, and how they interact with each other [6, p. 65]. Before using MD, it is necessary to make sure that the force field used accurately describes all the atoms and their interactions

for the studied system. This is called parametrization, and the process of how it is conducted has been the main focus in this thesis.

The aim of the research conducted here was to parametrize a Optimized Potentials for Liquid Simulations – All Atom [7] (OPLS-AA) -based force field for a organic solar cell donor–acceptor (D–A) copolymer benzo[1,2-*b*:4,5-*b*']dithiophene-thieno[3,4-*c*]pyrrole-4,6-dione (PBDT-TPD), and test the performance of this force field in MD simulations in solvent and in both crystalline and amorphous phases by comparing the results of these simulations to previous computational studies. The quantum mechanical (QM) optimizations required for the parametrization process were carried out with the Gaussian 09 software [8], and MD simulations with GROMACS software package [6]. In the previous studies, LAMMPS software [9] in references [10] and [11], or TINKER software [12] in reference [13] has been used in simulating the PBDT-TPD polymer. The force field parametrized in this thesis differs from these studies not only because it is made for GROMACS software [6], but also in the parametrization process, as explained in more detail in later chapters.

Including this introduction, this thesis in structured into seven chapters. Chapter 2 focuses on organic solar cells (OSC) and what should be known about their structure and working principle in the scope of this thesis. The theories behind the computational methods used in the thesis are divided into two chapters, with chapter 3 focusing on the classical MD methods and chapter 4 on the QM calculations. Chapter 5 explains how these computational methods were used in this thesis in the parametrization of the force field and in the simulations that were carried out with it. Chapter 6 covers the results of the work and their significance, with chapter 7 bringing the whole thesis to conclusion.

2. ORGANIC SOLAR CELLS

Many different types of materials have been used in solar cells during their short history. The market is still dominated by so called first generation solar cells, which are mainly based on silicon wafers and have power conversion efficienciens (PCEs) between 14 % and 19 %. They have a good performance and high stability, but both the manufacturing process and the materials are expensive. [14][15, p. 6–7]

Attempts for lower production costs have resulted in the second generation of solar cells, in which silicon wafers have been replaced with amorphous silicon, copper indium gallium selenide (CIGS) or cadmium telluride (CdTe). Unlike the first generation solar cells, they have a flexible structure and can be applied to many different surfaces. However the manufacturing processes of them still include expensive vacuum processes and high temperature treatments. The PCEs of these solar cells is between 9 % and 12 %. [15, p. 7]

The newest ones on the field are OSCs, which are the third generation of solar cells. Such are for example dye-sensitized solar cells, quantum dot solar cells, small molecule and PSCs. This thesis focuses mainly on PSCs. PSCs are an interesting alternative compared to solar cells of earlier generations because of their low production cost in the industrial scale and flexibility of the material. Their PCEs typically lie between 6 % and 8 %, but efficiencies of over 10 % have also been achieved [16]. While their performance can not yet compete with the traditional silicon based solar cells, PSCs are showing a lot of potential and continuous research is being done on developing them. [1][14][15, p. 7–8]

This chapter focuses on what should be known about PSCs and their function in the scope of this thesis. First the nature of light and its absorption by matter are explored in section 2.1. The structure of an OSC and the significance of different materials used in it are explored in section 2.2, and the working principle is explained in detail in section 2.3. The final section 2.4 of the chapter focuses on how the OSCs can be and have been studied with computational methods. This has been the focus in this thesis as well, as all work has been done computationally.

2.1 The nature of light

Solar cells generate electricity through the photovoltaic effect [17], which is a phenomenon that creates an electric current in a material when it is exposed to electromagnetic radiation [15, p. 6]. In the case of solar cells, this radiation is sunlight, and its energy is being converted into electrical energy. Electromagnetic radiation consists of electrical and magnetic fields oscillating simultaneously in planes perpendicular to each other at the speed of light, which is called an electromagnetic wave [18, p. 415]. Visible light that is mostly absorbed by solar cells is a small part of the whole electromagnetic spectrum illustrated in figure 2.1, with a wavelength in the range of 400–700 nm [19, p. 524]. The waves in electromagnetic radiation are characterized by wavelength and frequency according to equation

$$\lambda\nu = c, \tag{2.1}$$

where λ (nm) is the wavelength, ν (Hz) the frequency and c the speed of light which has the value of 299 792 458 (m/s) $\approx 3 \times 10^8$ (m/s) [19, p. 523]. As visible from figure 2.1, wavelength and frequency are inversely related, meaning that a wave with a higher wavelength will have a lower frequency, and vice versa. [18, p. 413–415]

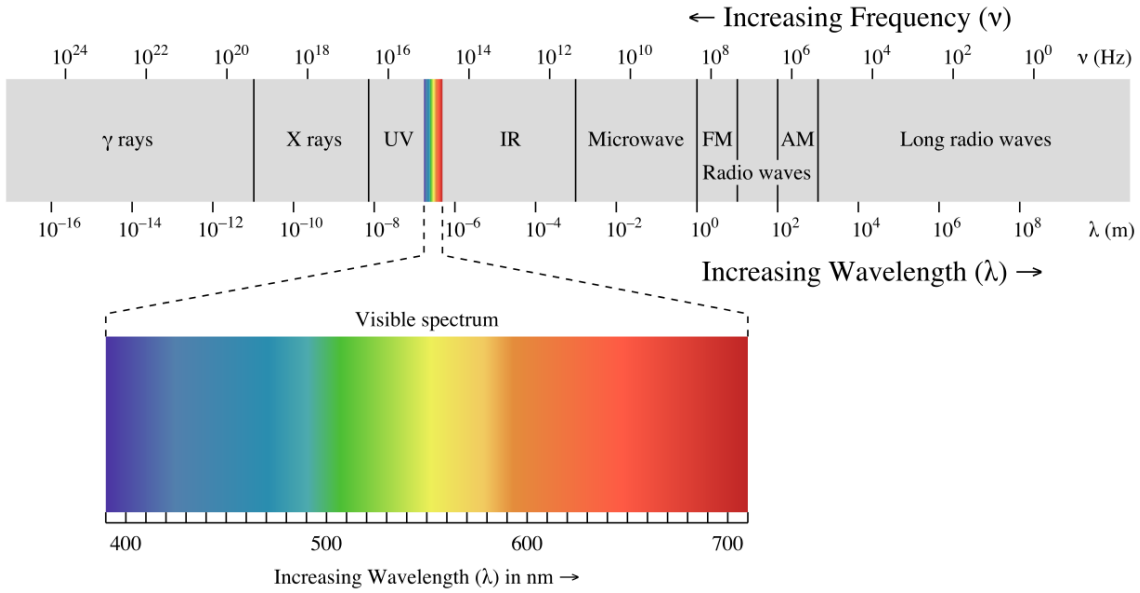

Figure 2.1 *The range of electromagnetic spectrum showing the different types of waves at their specific wavelength ranges. Licensed under CC-BY-NC-SA 3.0. [20]*

Even though the electromagnetic radiation consists of waves, in certain cases it shows also characteristics of particulate matter. This is referred to as the wave-particle duality [18, p. 283], which means that electromagnetic radiation can also be viewed as a stream of particles called photons, which are the elementary particles associated with the electromagnetic interaction of the four fundamental interactions [21, p. 571–574]. The mass of a photon is zero, and the energy of a photon E_{photon} is given by the equation

$$E_{photon} = h\nu = \frac{hc}{\lambda}, \tag{2.2}$$

where h is the Planck constant which has the value of 6.626×10^{-34} Js, with the other quantities remaining the same as they were previously in equation 2.1 [19, p. 526]. Another important postulate which is closely related to the equation 2.2, observed by the physicist Max Planck, is that energy can only be gained or lost by integer multiples of $h\nu$, which from equation 2.2 is known to be the energy of a photon. This means that energy is not continuous but quantized, meaning that transfer of any given amount of energy is not possible. Energy can only be transferred by integer amounts of $h\nu$, which is also called a quantum of energy. [19, p. 525–528]

When light interacts with matter, few different things may happen. Light can either be transmitted through the material, reflected from its surface or be absorbed by it, with absorption being the most of interest in the case of solar cells. When a molecule M absorbs a photon with a quantum of energy $h\nu$ according to equation 2.2, the energy transfers the molecule into an excited state M^*. This reaction is shown by equation [15, p. 5]

$$M + h\nu = M^*. \tag{2.3}$$

What this means is that the quantum of energy is used to transfer one of the electrons from the molecule to a molecular orbital that has a higher energy than the orbital the electron was previously occupying. This is called the HOMO–LUMO transition, and the acronyms stand for highest occupied molecular orbital and lowest unoccupied molecular orbital, respectively. The energy difference between the two orbitals is called the HOMO–LUMO gap, and the transition from HOMO to LUMO can only happen if the energy difference is equal to or lower than the quantum of energy $h\nu$ absorbed. HOMO–LUMO transition is being illustrated in figure 2.2.

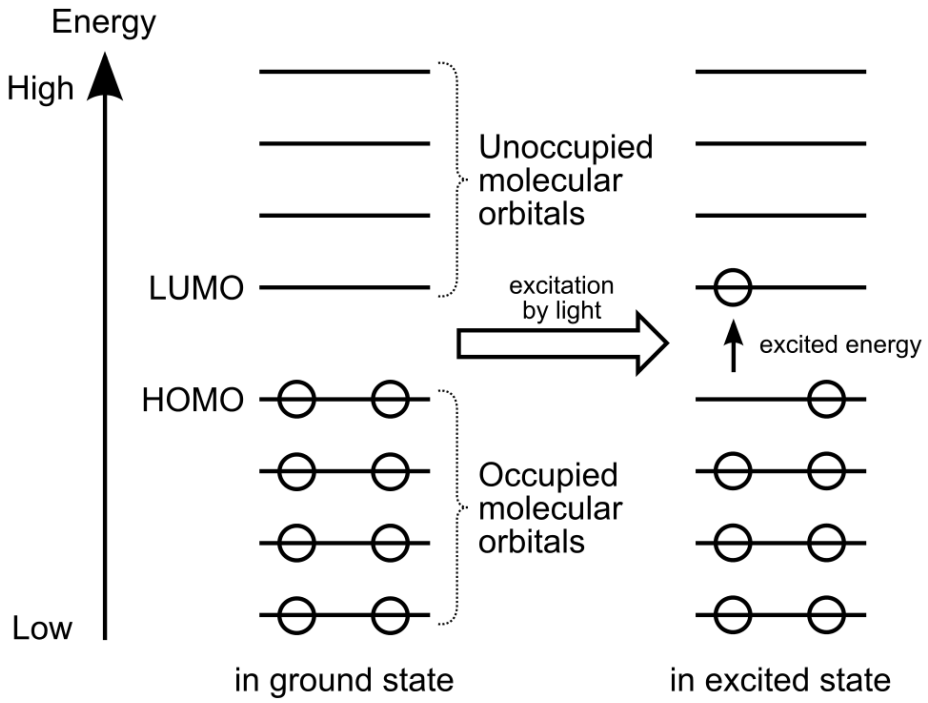

Figure 2.2 *The excitation of light transfers an electron from HOMO of a molecule to LUMO. [23]*

These excited states are also called excitons [15, p. 9] or electron–hole complexes, with hole meaning a positive charge caused by the absence of an electron. [18, p. 347–348][22]

2.2 Structure of a polymer solar cell

The most simple way to picture the structure of a solar cell is to say that it consists of two electrodes and between them a photoactive layer that is able to absorb photons and generate charges. When the material is of an organic substance, this structure depicts a single layer OSC, for which highest reported values of efficiency are around 0.3 % [15, p. 11]. Being the first example of organic photovoltaics they are quite inefficient and have been later replaced by more advanced devices, such as the bilayer heterojunction and bulk heterojunction (BHJ) solar cells. [3][4]

In a bilayer version the eD and eA materials are stacked next to each other in different layers, whereas as in BHJ cells, the eD and eA materials are mixed together to form an interpenetrating network. The structure of both of these versions is shown in figure 2.3. The efficiencies of bilayer heterojunction cells reach around 4 % and

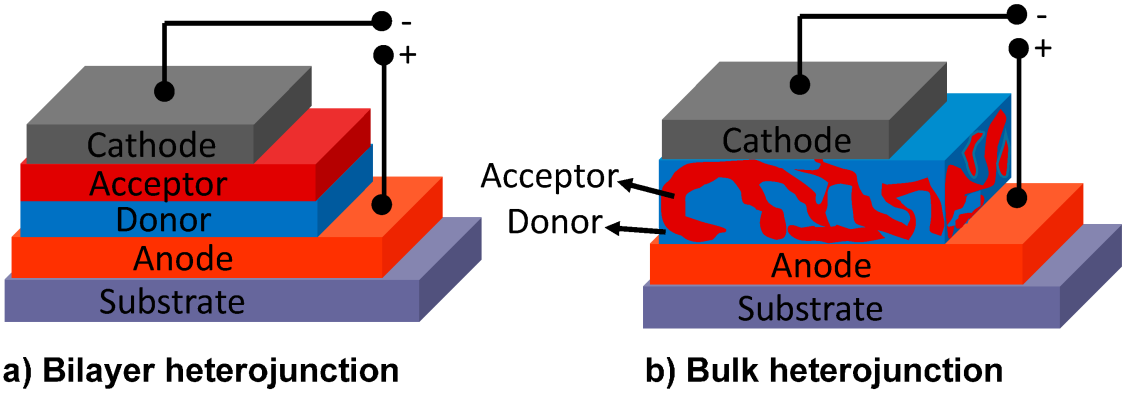

Figure 2.3 *The basic structures of an bilayer heterojunction and bulk heterojunction solar cells. Figure acquired from reference [26], MDPI Open Access.*

6 % [15, p. 10–11], and with BHJ cells as high as 10 % [24]. In both cases the charge transfer and separation, which are important steps in the working principle of these solar cells, take place on the interface between the eD and eA materials. This surface area is larger in BHJ cells, which enhances the charge separation and maximizes the contact area between the eD and eA layers, which results in better performance of BHJ cells compared to bilayer heterojunction cells. [22][25]

The idea of layers can be extended further by adding more of them to create multi-layered solar cells. BHJ cells often contain electron and hole trasporting buffer layers that contribute to better overall efficiency of the solar cell for example by improving charge transport from the organic material to the electrodes [27]. Tandem solar cells that contain multiple active layers also exists [28][29]. The different main functional parts of the organic solar cells, the materials used, their purpose and significance is being discussed in the following subsections.

2.2.1 Substrate material

Substrate is the layer on which all other parts of the device are attached to. No reactions happen in the substrate, its function is to be a supporting structure for the other parts of the solar cell, and to prevent oxygen and water from diffusing into the device. Other desired properties are transparency for the light to pass through and thermal stability to sustain high processing temperatures. Most commonly used substrate material is glass. Glass is used because it is inexpensive and it is commercially available precoated with a common anode material indium tin oxide (ITO). Plastic such as polyethylene terephthalate (PET) can also be used, their benefits being light weight and flexibility. [27]

2.2.2 Transparent electrode

Transparent electrode is deposited on top of the substrate material, and as mentioned in the previous section, the most commonly used anode material is ITO, which is a semiconductor with a wide bad gap E_g, typically in the range of 3.2–4.3 eV [30]. This band gap covers approximately 85 % of the spectrum of visible light, which allows the active organic layer to efficiently absorb photons [27]. Yet another advantage of ITO is its work function Φ_f, which lies in the broad range of 3.7–5.1 eV, and which can be fine-tuned to match the energy levels of the adjacent organic materials by various surface treatment methods [31].

2.2.3 Active layer

The active layer is sandwiched between two electrodes that have different work functions. Different types of organic molecules can be used as photoactive materials the active layer, but in the PSCs typically conjugated polymers are used as eD materials, and fullerene derivatives as eA materials. For a better performance, it is desireable to narrow E_g and to fine-tune the energy levels of the conjugated polymer. This can be done by using the D–A approach [32]. To avoid confusion between the two similar terms, in this thesis donor D and acceptor A refer to the building blocks within the conjugated polymer, and electron donor eD and electron acceptor eA refer to the whole polymer donor and fullerene derivative acceptor, respectively. [4][33][34]

With the D–A approach, the idea is to use alternating electron rich donor and electron deficient acceptor units in the repeating unit of the D–A copolymer [32]. Generally the structures of the D and A units contain 5- and 6-membered rings that are fused together, because that improves the planarity of the polymer, which affects the charge transfer [4]. Molecules such as thiophene, bithiophene and benzodithiophene (BDT) are used as strong donor units, and naphthalane diimide, benzothiadiazole and thienopyrroledione (TPD) as acceptor units [4]. The conjugated polymer backbone is the most important part of the design of solar cell polymers, but side chains and substituents also play a part in improving and tweaking their physical properties, such as solubility, molecular weight and energy levels [34].

After polymerization, the HOMO of the D moiety will interact with the HOMO of the A moiety, which creates two new HOMOs. The same thing happens with the LUMOs of the different moieties creating two new LUMOs. The electrons redistribute to the new hybridized orbitals of the D–A copolymer, a higher HOMO and

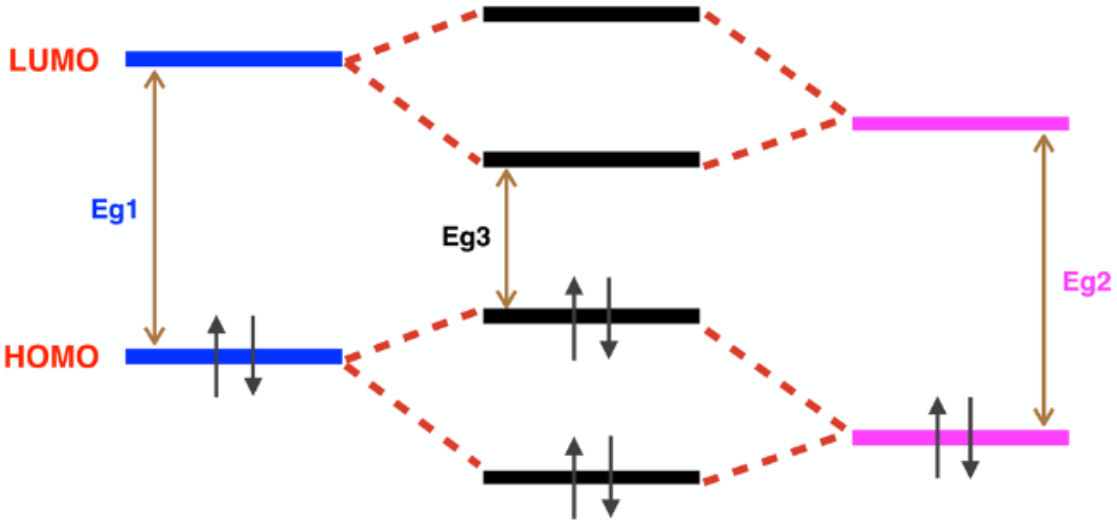

Figure 2.4 *Illustration of the HOMO–LUMO gap (E_g) narrowing by D–A interaction. Adapted with permission from [4]. Copyright (2015) American Chemical Society.*

lower LUMO energy levels are created. This leads to a narrower HOMO–LUMO gap. The mechanism for this is shown in figure 2.4. [4][34]

2.2.4 Metal electrode

On the other side of the active layer a metal electrode is deposited to be used as the cathode. The work function of the cathode needs to be lower than that of the anode material to cause an electric field inside the device which promotes hole collection at the anode and electron collection at metal cathode. Metals with an ideal work function are for example silver 4.3–4.7 eV and aluminium 4.2 eV. What also needs to be considered is to align the energy levels so that the metal work function is almost equal to the LUMO energy of the acceptor material. This allows for efficient collection of electrons at the cathode. Finally, the metal electrode also plays a role in reflecting unabsorbed light back through the device. In principle this means that the thickness of the active layer is effectively doubled, because light can be absorbed when it is travelling through the device in either direction. [27]

2.3 Working principle of a polymer solar cell

The conversion of light into electricity in the organic solar cell can be divided into four consecutive steps. These are the (i) absorption of photon by the eD, which forms an exciton, the (ii) diffusion of the exciton to the eD–eA interface, where (iii)

charge separation occurs. Lastly (iv) charge transport to the anode and cathode causes an electric current between the electrodes. [3]

An exciton is created in the photoactive layer by an absorption of photon, as discussed in section 2.1. The excitons formed have an average lifetime shorter than 1 ns in PSCs [2]. During this time they have to be able to travel to the eD–eA interface. The distance the excitons have to travel is called the diffusion length, which in PSCs is approximately 10 nm. The distance between the donor and acceptor phases must be smaller than this diffusion length, or the excitons recombine back to the ground state before charge separation occurs at the eD–eA interface. This charge recombination is an undesired process because it lowers the performance of the solar cell. [3]

Requirements for the desired charge transfer to take place are a short distance and a suitable orientation between the two phases. The energy difference between the molecular orbitals involved in the reaction must also be suitable. For the reaction to happen, the energy of the final state where the charge will be transferred must be lower than the energy of the initial excited state [15, p. 5–6]. The charge transferred can be either an electron or a hole, and both the reactions are given by equations

$$\begin{aligned} eD^* + eA &\rightarrow eD^+ + eA^- \\ eD + eA^* &\rightarrow eD^+ + eA^- \end{aligned} \tag{2.4}$$

where the upper reaction represents electron transfer and the lower one hole transfer. [2][35][36]

When the exciton dissociates at the eD–eA interface, the electrons move to the acceptor phase and the holes to the donor phase. Both phases must form a continuous network that will connect them to the electrodes, so the charges can be transported to them. As mentioned previously, the difference in work functions in the used electrodes causes an electric field inside the device, which causes the electrons to move the cathode and holes to the anode. This causes an electric current in the device. [36]

The morphology of the active layer is therefore very important for the optimum performance of the solar cell for multiple reasons. The surface area between the donor and acceptor phases must be large to maximize the places for the charge separation between eD and eA. The distance between the phases must be smaller

than the diffusion length to avoid charge recombination back to the ground state. Both of these things enable as many excitons as possible to dissociate into electrons and holes. The network of the different phases must also be continuous, so that after the charge separation the charges may be transferred to the electrodes. Optimizing the structure of the active layer is an ongoing challenge in the field. [2]

2.4 Computational studies of donor–acceptor copolymers

A better understanding of the active layer is the way to achieve even better performance for PSCs, because as explained in the previous chapter, the morphology of the active layer is critical for the working principle of BHJ PSCs. Generally the goal is to understand the relationship between structure and property, how different polymer backbones, their side chains and substituents, and processing conditions affect the morphology of the active layer, and in turn how this active layer structure defines the properties of the solar cells. [5]

One possible approach for studying the active layer morphology is by computational methods, as they provide information on a molecular scale. These can either be QM methods such as density functional theory (DFT) calculations explained in chapter 4, or rely on classical mechanics like MD which is explored in chapter 3. Computational methods can prove very valuable, because from them insight can be gained on how relative orientations and interactions between the eD and eA molecules at their local interfaces affect the formation of the active layer morphology [5]. Especially when combined with experimental research methods, accurate interpretations of structure–property relationships can be achieved [37].

This is why active layer materials have been widely studied computationally, and examples of different researches conducted are summarized in the next paragraphs. The QM methods are focused on evaluating individual properties of the molecule such as electronic structures and excited state characteristics, while MD methods can be used to study packing morphology of the active layer on a larger scale, which is out of reach of QM calculations. However, both methods complement and work in conjunction with each other. For example, QM methods are used in evaluating parameters for a force field, used in the MD simulations, and the configurations acquired from the results of these MD calculations can again be used as in QM calculations, to study the local intermolecular properties at the more accurate level of theory [5]. The focus in this thesis is on DFT calculations that are used in the force field parametrization and MD simulations that are be carried out with the modified OPLS-AA style force field.

Previous studies of PSCs with MD have focused on the packing and interactions of the active layer. For example, Jackson et al. [13] parametrized a force field based on OPLS-AA [7] for the TINKER software [12] for 15 different D–A copolymers common in PSCs. They studied the conformational classes and aggregation behaviour of these D–A copolymers with MD by simulating single polymers with 30 constitutional repeating units (CRU) in implicit solvent with a background relative permittivity of chlorobenzene ($\epsilon_r = 10$). They also investigated the role of different solvents used in the processing conditions of PSCs and how they affect the packing of these polymers by simulating single tetramers in explicit solvents of both chloroform and chlorobenzene. In a later study, Root et al. [38] used the same modified force field with LAMMPS [9] to study the morphologies of three different D–A copolymers and their blends with the eA fullerene derivative $PC_{71}BM$ during the manufacturing process of PSCs. They used amorphous systems consisting of 60 chains with 12 CRUs. These systems were simulated in elevated temperatures of 800 K and cooled down to room temperature to simulate the melt-quenched morphologies, which were compared to the self-aggregated systems obtained by simulating the same systems only in room temperature.

In other studies, Caddeo et al. [39] used a General Amber Force Field (GAFF) [40][41][42] as a basis for their modified force field for a naphthalenediimide-thiophene -based P(NDI2OD–T2) D–A copolymer, and used the NAMD [43] software in the simulations. They studied simulated a single polymer with 18 CRUs in vacuum, a single polymer with 16 CRUs in both toluene and chloronaphtalene solvents, and a bulk phase consisting of 24 decamers in a crystalline phase. Do et al. [44] used LAMMPS software [9] and a modified OPLS-AA force field [7] in the simulations of benzodithiophene-thiophene copolymers PBDT[2H]T and PBDT[2F]T polymers. They simulated both polymers in amorphous systems that consisted of 80 pentamers, and investigated how fluorine substituents affect the conformation and packing of the polymer during the manufacturing process of the PSCs. This was done by first simulating the systems in an elevated temperature of 550 K, and then in the course of 10 ns linearly cooling them to temperature 298 K.

The D–A copolymer PBDT-TPD studied in this thesis has been the main focus in a few different computational articles [10][11][13]. Ravva et al. [10] parametrized a OPLS-AA -based force field [7] for LAMMPS software [9]. They studied the interactions between the D–A copolymer and the eA fullerene (C_{60} and $PC_{61}BM$) phase, and how different side chains (linear tetradecyl $C_{14}H_{29}$, linear octyl C_8H_{17} and branched 2-ethylhexyl C_8H_{17}) in the polymer affect them. Their systems consisted of a single C_{60} or $PC_{61}BM$ molecule and a single octamer PBDT-TPDs with different

side chains in chloroform. Larger systems which contained a single different PBDT-TPD octamer and 762 $PC_{61}BM$ molecules (or 616 in the case of 2-ethylhexyl and octyl side chains) were also studied. For these systems the manufacturing process was also taken into account by first simulating the polymer in a higher temperature 650 K and then cooling down the system to 300 K. This was also the focus in a more recent study of the same group, in Wang et al. [11], where the same modified force field and LAMMPS [9] software were used to investigate systems consisting of 30 PBDT-TPD chains with 18 CRUs with different side chains and 778 $PC_{61}BM$ molecules (or 629 in the case of 2-ethylhexyl and octyl side chains). As with the previous study, these amorphous systems were simulated at first in an elevated temperature 650 K and cooled down to temperature 300 K. The study also included simulations of single octamers in chloroform.

In this work the OPLS-AA force field [7] was used as a template for building the modified force field, according to procedure explained in chapter 5.1, for the MD simulations of PBDT-TPD with GROMACS [6]. The performance of the force field was tested by simulating a single octamer in chloroform and six octamers in vacuum in both crystalline and amorphous phases, as explained in more detail in chapter 5.2 and 5.3. The differences in the modified force field parametrized in this thesis compared to those of the previous studies, and results of these simulations are explored later in chapter 6.

3. MOLECULAR DYNAMICS

Molecular dynamics simulations are one of the ways different compounds and systems can be modelled. In these simulations Newton's equation of motion is used to calculate a *trajectory*, which is a representation of the movement of atoms in the system as a function of time. Because Newton's laws are used in the calculation, this means that the simulation is based on classical mechanics. Quantum mechanical phenomena such as breaking and formation of new chemical bonds does not occur, only the conformations of the molecules change. MD is based on an algorithm, which is shown in figure 3.1. [6, p. 2–3][45, p. 139–140].

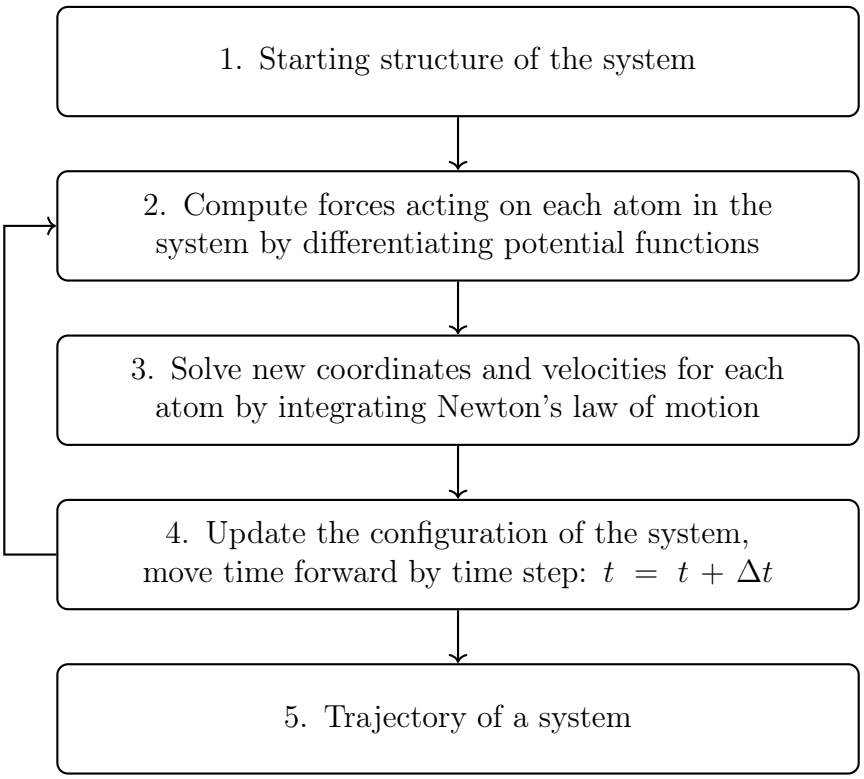

Figure 3.1 *The common algorithm that MD is based on. Adapted from picture 3.3 in reference [6, p. 16].*

Simulation begins with the starting configuration of the system, which contains necessary information about the properties of the different atoms in the system. These properties are discussed in detail in the next subsection 3.1. Next the total force acting on each atom in the system is calculated. This is done by differentiating potential functions, which represent how different atoms interact with each other. These different potential functions are included in the force field, which is discussed in subsection 3.2. After this the forces are used to compute new positions and velocities for each atom. This calculation is done by numerically integrating Newton's second law of motion over the given time step Δt. This part of the simulation process is explained in subsection 3.4. After this the configuration of the system is updated with the new positions and velocities for atoms, and time is moved forward by time step. Then the steps 2, 3 and 4 shown in figure 3.1 are repeated. The time step is the time interval between two of these consecutive calculation loops. The loop is repeated until a simulation of a desired time length is achieved. Mathematically the whole algorithm can be presented with an equation

$$m_i \frac{d^2 \mathbf{r}_i}{dt^2} = \mathbf{F}_i = -\frac{\partial U_{TOT,i}}{\partial \mathbf{r}_i}, \qquad i = 1, 2, \ldots, N, \tag{3.1}$$

where for each atom i mass is m_i, location vector $\mathbf{r}_i$ and force vector $\mathbf{F}_i$. U_{TOT} describes the sum of different potential functions acting on the atom and t is time [6, p. 2]. When equation 3.1 is performed for each atom $i = 1, 2, \ldots, N$ contained in the system for as many calculation loops as desired, the product of the simulation is a trajectory for the studied system. It contains the coordinates and velocities of atoms as a function of time, and various phenomena can be observed or different quantities can be calculated from it. [6, p. 16][46, p. 6–7]

In this thesis, the MD simulations have been carried out with the GROMACS software package and therefore this chapter has been written from the perspective of GROMACS. Unless specifically stated otherwise, all the information in the following subsections is based on the GROMACS User Manual version 2016.3 [6].

3.1 Structure of the system

The simulation begins with defining the structure of the system, for which the coordinates and velocities for each atom in the molecule are required. The coordinates define the location of each atom in a three-dimensional space, and they can be acquired by building the molecule in a modelling software. The velocities for atoms are

also needed for the calculation. In their absence GROMACS generates the velocities in a given temperature by using the Maxwell–Boltzmann distribution function

$$P(v_i) = \sqrt{\frac{m_i}{2\pi k_B T}} \exp\left(-\frac{m_i v_i^2}{2k_B T}\right), \tag{3.2}$$

where P is the probability to obtain a velocity v_i for an atom with a mass of m_i. k_B is the Boltzmann constant and T the given temperature in Kelvin. [6, p. 17]

With the positions and velocities for the atoms acquired, the properties of the atoms themselves also need to be defined. Individual atoms in the molecules have different masses and charges based on their elements, and these have to be determined. This is illustrated by pictures 3.2 and 3.3. [6, p. 117–118]

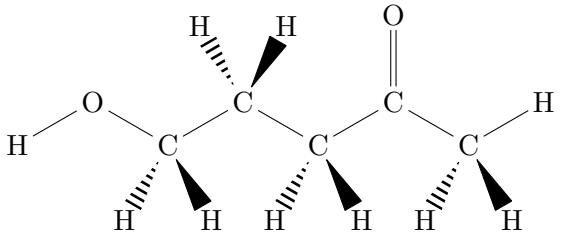

Figure 3.2 *Structural formula of a 5-hydroxy-2-pentanone showing all the different atoms in the molecule.*

Figure 3.2 shows the structural formula of a relatively simple 5-hydroxy-2-pentanone molecule containing three elements, carbon, hydrogen and oxygen. The masses of the different atoms of the same element differ if they have different isotopes, but this aspect is often not taken into account. This is because basically everything observed from the simulations is based on electromagnetic interaction, and the charges are a much more important property to define accurately than the masses.

While determining charges, it is important to note that not all atoms of the same element share the same electromagnetic properties. For example the for the compound shown in figure 3.2, the carbonyl carbon will have different partial charge compared to other carbon molecules in the compound, because it is bound to an electron-withdrawing oxygen atom. In GROMACS, the atoms in the molecules are divided into different atom types based on their bond types and electromagnetic properties. Different atom types for the previously shown 5-hydroxy-2-pentanone are shown in figure 3.3. [6, p. 117–118]

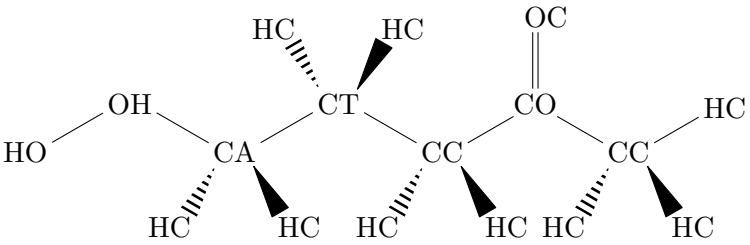

Figure 3.3 *Structural formula of 5-hydroxy-2-pentanone showing all the different atom types in the molecule. For this example, the names for the different atom types are arbitrary, and not all of them correspond to those of the OPLS force field.*

In figure 3.3, the carbon atoms are divided into three different atom types, CT for a alkane carbon, CO for a carbonyl carbon, CC for the carbons bonded to the carbonyl carbon and CA for a carbon bonded to the hydroxyl group. Similarly the two oxygens in the molecule have different atom types because they are in different functional groups. The carbonyl oxygen is given the atom type OC and hydroxyl oxygen atom type OH. Also the hydrogen in the hydroxyl group HO is different from the alkane hydrogens HC.

Lastly the interactions between the different atoms have to be defined. GROMACS uses a topology file to do this, and in it the three different bonded interactions required are bonds, angles and dihedrals. Bonds simply tell which two atoms are bonded to each other with a covalent bond. Angles depict the interaction between three adjacent bonded atoms. Dihedrals are a combination of four atoms that describe the rotational behaviour of a bond, and they are divided into so called proper and improper dihedrals. These different interactions are discussed in detail in the next section. [6, p. 65]

3.2 Force fields

A force field contains potential equations which describe the different types of interactions between the atoms in the system. There are many different types of force fields which can be used for the simulations, and by default the GROMACS software package is compatible with 15 different ones. In this work the OPLS-AA (Optimized Potentials for Liquid Simulations - all atom) force field was used as the base for the modified force field. The OPLS-AA contains five different potentials, which means five different ways how the atoms can interact with each other. Three of these depict chemical bonded interactions and the remaining two are used to describe long range interactions between atoms. The total potential U_{TOT} of an atom in the system is

obtained as a sum of the bonded potentials U_{bonded} and the non-bonded potentials $U_{non-bonded}$ [6, p. 65]

$$U_{TOT} = U_{bonded} + U_{non-bonded}. \tag{3.3}$$

In addition to the these potentials, restraints can be included to complement the interactions. They are used to impose restraints on the motion of the atoms, such as their position and orientation, either to avoid disruptive deviations, or to include knowledge from experimental data. In practice, they are often used in equilibration of the system before the real simulation. Restraints are based on fixed lists and automatically generated by GROMACS, and with the exception of restraining one dihedral angle during the parametrization process, they are generally not modified or focused on during the MD calculations. Therefore the form of these restaints is not of interest in the scope of this thesis and they are therefore not explored further, more information can be found in the GROMACS user manual [6, p. 84–94]. The next two subsections deal with the different types of potential functions in the OPLS-AA force field.

3.2.1 Bonded interactions

As stated previously, all the covalent bonds between the atoms in the system are defined in the topology file. Bonded potentials are described by interactions between two, three, or four atoms. The different interactions are bond stretching U_{bonds}, angle bending U_{angles}, and dihedrals $U_{dihedrals}$, which includes both the proper dihedral angle torsion and improper dihedral out of plane bending. The total bonded potential acting on an atom is the sum of these three potentials [6, p. 71]

$$U_{bonded} = U_{bonds} + U_{angles} + U_{dihedrals}. \tag{3.4}$$

Bond stretching occurs between two atoms i and j that are covalently bonded to each other. This is illustrated in figure 3.4. The potential U_{bonds} is calculated according to a formula [45, p. 154–155]

$$U_{bonds}(r_{ij}) = \frac{1}{2}k^b_{ij}(b_{ij} - b^0_{ij})^2, \tag{3.5}$$

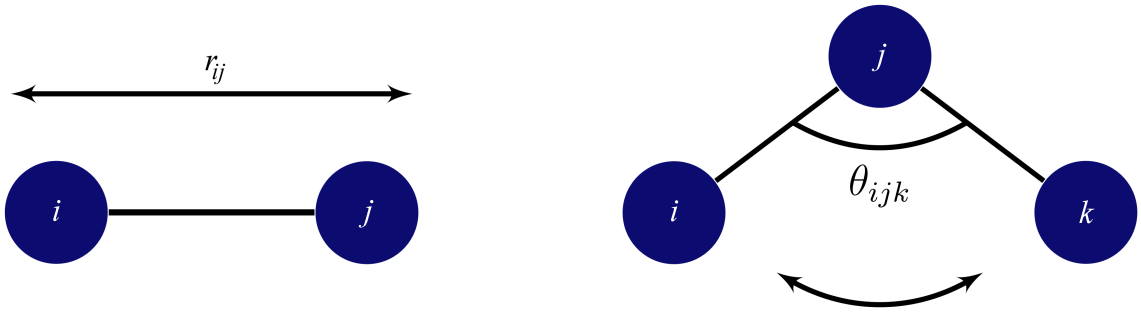

Figure 3.4 *Bond stretching between atoms i and j on the left, and angle bending between a triplet of atoms i, j and k on the right.*

where k^b_{ij} (kJ mol^{-1} nm^{-2}) is a bond force constant, b_{ij} (nm) the bond length and b^0_{ij} (nm) the reference bond length [6, p. 71]. The bond length varies during the course of the simulation, but both the force constant and the reference bond length are parameters which are included in the force field for each different atom type pair that forms a bond in the studied molecule. Equation 3.5 is a harmonic potential, which means that the bond stretching is modelled as a spring. This is a computationally efficient and an adequate way to model the potential, and it is used in many different force fields [42][47][48]. In case the system requires the use of an anharmonic bond stretching potential, the Morse potential [49] can be used. [46, p. 25–27]

Angle bending potential is calculated for three atoms i, j and k. As presented in figure 3.4, marking of the atoms is in a sequence of covalently bonded atoms, with atom j being in the middle and i and k at the ends. This potential U_{angles} is also presented as a harmonic potential [45, p. 154]

$$U_{angles}(\theta_{ijk}) = \frac{1}{2}k^{\theta}_{ijk}(\theta_{ijk} - \theta^0_{ijk})^2, \tag{3.6}$$

where k^{θ}_{ijk} (kJ mol^{-1} rad^{-2}) is the angular force constant, θ_{ijk} (deg) is the angle between the atoms and θ^0_{ijk} (deg) the angle reference value for this angle [6, p. 74]. Angles in the force field files are given in degrees, but GROMACS internally converts them to radians for the calculation. As in the bond stretching potential, the angle between the atoms varies in the simulation, and both the angular force constant and the reference angle value are constants defined in the force field. Both have their own characteristic values for each different triplet of atom types. Angle bending can also be modelled by a potential that uses a fourth order polynomial, if

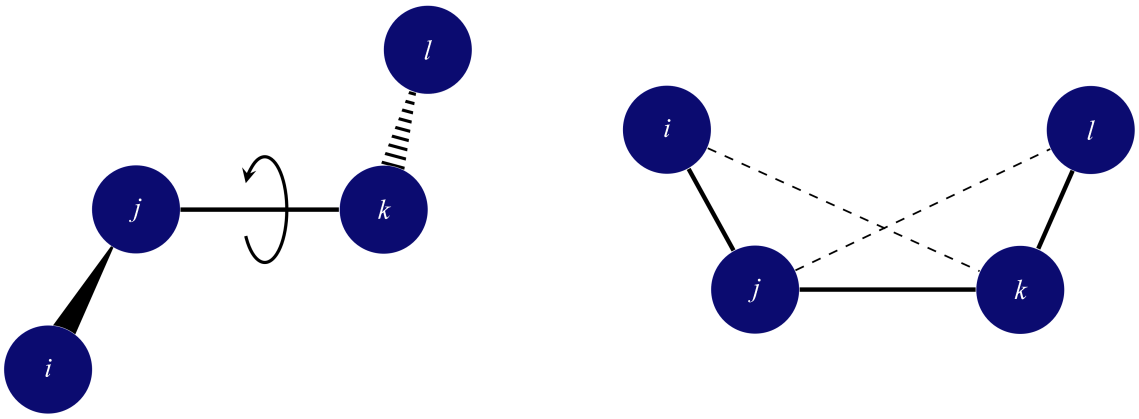

Figure 3.5 *On the left, proper dihedral angle torsion of the bond between atoms j and k. The dihedral angle is defined as the angle between the plane formed by atoms i, j, and k, and the plane formed by atoms j, k, and l. On the right, improper dihedral out of plane bending.*

a more accurate description is desired. This is special case though and the harmonic potential is the most commonly used one in different force fields. [46, p. 27–30]

Dihedrals describe potentials between a series of four bonded atoms i, j, k, and l. They are divided to proper and improper dihedrals, and the total dihedral potential is acquired as their sum

$$U_{dihedrals} = U_{propers} + U_{impropers}. \tag{3.7}$$

Proper dihedrals [6, p. 79–81] describe the angle torsion of the bond between atoms j and k, as shown in figure 3.5. The potential for proper dihedrals is calculated by a Ryckaert–Bellemans function [45, p. 155]

$$\begin{aligned} U_{propers} = U_{RB}(\psi) &= \sum_{n=0}^{5} C_n(\cos(\psi))^n \\ &= C_0 + C_1\cos\psi + C_2\cos^2\psi + C_3\cos^3\psi + C_4\cos^4\psi + C_5\cos^5\psi \end{aligned} \tag{3.8}$$

where ψ is the dihedral angle (deg), and C_0–C_5 (kJ mol^{-1}) are six coefficients defined in the force field for each dihedral that contains a different quartet of atom types [6, p. 80–81]. The Ryckaert–Bellemans function 3.8 can also be expressed by so called Fourier dihedrals by equation

$$U_{RB}(\phi) = \frac{1}{2}\Big(F_1(1+\cos(\phi)) + F_2(1-\cos(2\phi)) + F_3(1+\cos(3\phi)) + F_4(1-\cos(4\phi))\Big). \tag{3.9}$$

The F_n constants in the equation 3.9 are calculated from the C_n constants of the Ryckaert–Bellemans dihedrals by GROMACS, because this is more efficient. The basis for the conversion is shown in the GROMACS User Manual [6, p. 80–81]. It should also be noted that GROMACS uses the units of kJ mol^{-1} for the RB parameters, and OPLS parameters in literature are given in units of kcal mol^{-1}. [6, p. 81]

A special case for dihedrals is when all the four atoms forming the dihedral are in the same plane. These are called improper dihedrals [6, p. 77–79], and they are used to keep planar groups such as aromatic rings and their substituents planar. They are also used to preserve the chirality of the molecules by preventing double bonds from flipping over to their mirror images. An example of an improper dihedral is represented in figure 3.5. Improper dihedral potential is calculated as a harmonic potential according to equation [45, p. 155]

$$U_{impropers}(\xi_{ijkl}) = \frac{1}{2}k^{\xi}_{ijkl}(\xi_{ijkl} - \xi^{0}_{ijkl})^2 \tag{3.10}$$

where k^{ξ}_{ijkl} (kJ mol^{-1} rad^{-2}) is the improper dihedral force constant, ξ_{ijkl} (deg) the dihedral angle between the atoms and ξ^{0}_{ijkl} (deg) the reference value for the dihedral angle. Again, the angle values are given in degrees in the force field files, but for the calculation they are converted to radians by GROMACS. [6, p. 77]

3.2.2 Non-bonded interactions

Non-bonded interactions [6, p. 65–71] are calculated for two atoms that are not covalently bonded but are within a certain distance of each other. These long-range interactions are described by the electrostatic Coulomb potential $U_{Coulomb}$ and by the Van der Waals interaction, which is most commonly represented by the Lennard-Jones potential $U_{Lennard-Jones}$. The total non-bonded interaction is acquired as the sum [45, p. 156]

$$U_{non-bonded} = U_{Coulomb} + U_{Lennard-Jones}. \tag{3.11}$$

The Coulomb interactions is calculated between two charged atoms i and j, and it is given by equation [45, p. 155][50, p. 291–292]

$$U_{Coulomb}(r_{ij}) = \frac{q_i q_j}{4\pi\epsilon_0\epsilon_r r_{ij}} \tag{3.12}$$

where q_i and q_j are the charges of atoms i and j, ϵ_0 the vacuum permittivity, ϵ_r the relative permittivity and r_{ij} (nm) the distance between the two atoms [6, p. 67]. In GROMACS, the charges q are defined individually for each atom and are therefore not necessarily the same for all atoms of the same atom type. The Coulomb potential is inversely proportional to the distance r_{ij}, so the further apart the atoms are from each other the weaker the potential is.

The Lennard-Jones potential that is used to model non-electrostatic Van der Waals interactions contains a short-range repulsion term and a long-range attraction term between the two atoms. Like the Coulomb potential, the Lennard-Jones potential is also inversely proportional to the distance r_{ij}. It is given by equation [45, p. 155][51, p. 30]

$$U_{Lennard-Jones}(r_{ij}) = 4\epsilon_{ij}\left(\left(\frac{\sigma_{ij}}{r_{ij}}\right)^{12} - \left(\frac{\sigma_{ij}}{r_{ij}}\right)^{6}\right), \tag{3.13}$$

where parameters ϵ_{ij} (kJ mol^{-1}) and σ_{ij} (nm) are parameters defined for the two atom types for which the interaction is being calculated [6, p. 66]. In the OPLS-AA force field they are calculated according to equations

$$\begin{aligned} \epsilon_{ij} &= (\epsilon_{ii}\epsilon_{jj})^{1/2} \\ \sigma_{ij} &= (\sigma_{ii}\sigma_{jj})^{1/2}, \end{aligned} \tag{3.14}$$

where ϵ_{ii} and ϵ_{jj} are the ϵ parameters defined in the force field for the atom types i and j, and σ_{ii} and σ_{jj} are the σ parameters for the atom types i and j, respectively [6, p. 66–67].

These non-bonded potentials could from a mathematical point of view be calculated between any two atoms in the system. However after a certain distance this would be pointless, because with increasing the distance the non-bonded potentials approach

zero and their significance on the total potential decreases. This is why GROMACS uses a so called cut-off radius for both the Coulomb and Lennard-Jones interactions. Beyond this cut-off radius the long-range interactions are set to zero and are no longer calculated. This is a useful practice that saves both time and computational resources. [6, p. 3–4]

3.3 Energy minimization

Before the actual simulation, the system is often energy minimized. This is because the initial starting structure is usually too far away from equilibrium or a local energy minimum to allow actual dynamics to be calculated. In the beginning the molecules in the system tend to be too close to each other, causing the calculated forces to become excessively large, which often leads to a failure in the MD simulation. To avoid this energy minimization algorithms are adopted, and their point is to relax the system before the real dynamics simulations. [50, p. 437]

The algorithm used in this work for the minimization was the *steepest descent* algorithm [6, p. 49–50]. The idea of the method is to use derivative information from the potential energy function and follow the direction of the negative gradient, which is the same as the direction of the driving force. The nearest local minimum is therefore found by moving along the steepest local gradient of the energy function. In the method forces and the potential energy is calculated first, and mathematically it can be expressed by equation

$$\mathbf{r}_{n+1} = \mathbf{r}_n + \frac{\mathbf{F}_n}{\max(|\mathbf{F}_n|)} d_n, \tag{3.15}$$

where $\mathbf{r}_{n+1}$ is the new positions for the atoms, $\mathbf{r}_n$ the initial position, $\mathbf{F}_n$ the force, or the negative gradient of the potential, $\max(|\mathbf{F}_n|)$ the largest absolute value of the force components and d_n the maximum displacement [6, p. 50]. The minimization stops when the algorithm has been run as many steps as user has set, or when absolute value of the maximum force is smaller than a specified value, which can again be set by the user. After the system has been relaxed with energy minimization, the simulation of the real dynamics can begin.

3.4 Integrating Newton's second law of motion

The total potential U_{TOT} on the atom i at a location $\mathbf{r}_i$ at a given time is calculated as a sum of the different potentials according to equation 3.3. The total force $\mathbf{F}_i$ acting on this atom can be solved from a formula 3.1

$$\mathbf{F}_i = -\frac{\partial U_{TOT}}{\partial \mathbf{r}_i}. \tag{3.16}$$

With the force calculated, the new location coordinates and velocities for the atom can be solved according to Newton's second law of motion $F = ma$, which can also be written as

$$\frac{d^2\mathbf{r}_i}{dt^2} = \frac{\mathbf{F}_i}{m_i}, \tag{3.17}$$

which is also presented in equation 3.1. From equation 3.17, the new location and the velocity vectors are acquired by numerical integration. The two most common algorithms used in the integration are the *leap-frog* and *Verlet* algorithms [52], with *leap-frog* being the default integrator used by GROMACS and also the one used in this work. [6, p. 26]

In *leap-frog*, the locations $\mathbf{r}_i$ are solved at time t and velocities $\mathbf{v}_i$ at time $t - \frac{1}{2}\Delta t$ according to the equations

$$\mathbf{v}_i(t + \frac{1}{2}\Delta t) = \mathbf{v}_i(t - \frac{1}{2}\Delta t) + \frac{\Delta t}{m_i}\mathbf{F}_i(t) \tag{3.18}$$

$$\mathbf{r}_i(t + \Delta t) = \mathbf{r}_i(t) + \Delta t\mathbf{v}_i(t + \frac{1}{2}\Delta t), \tag{3.19}$$

where Δt is the used time step, m_i the mass of the atom i, and F_i the total force acting on it. Even though the calculation for both the location and the velocities is being done simultaneously, the interval $\frac{1}{2}\Delta t$ between the equations makes the calculation alternate between the two. [6, p. 26]

This calculation is done for every atom in the system. After the integration all the atoms in the system are moved to their new locations according to the calculations, the velocities are updated, and the time is moved forward by the time step. The

new configuration for the system is now ready, and the loop presented in figure 3.1 is started from the beginning. Once again the total potential acting on each atom is solved, the total force is calculated by differentiating the total potential, and new coordinates and velocities are solved by integrating the Newton's second law of motion. The configuration is updated, and the loop started again. Once the system has been simulated for the desired time, a trajectory for the system is obtained, and the results of the simulation can be analysed from it. [6, p. 16]

3.5 Simulation box and periodic boundary conditions

For the simulations, the studied system is placed in a simulation box, which is a three-dimensional space that defines the area where the calculation will take place. Simulation boxes come in different shapes depending on the system, but cubic and triclinic ones are the most common ones. Even though this box defines the boundaries of the system, this does not usually mean that the simulated system reaches an artificial wall near the ends of the box. To avoid the effect of artificial edges or the interaction of the system with vacuum, periodic boundary conditions (PBC), illustrated in figure 3.6, are often adopted. Simulations that take place in a vacuum are an exception, and in these cases periodic boundary conditions should not be used, and the size of the simulation box should be excessively large, so that the molecules do not reach the edges of the box. [6, p. 11–14]

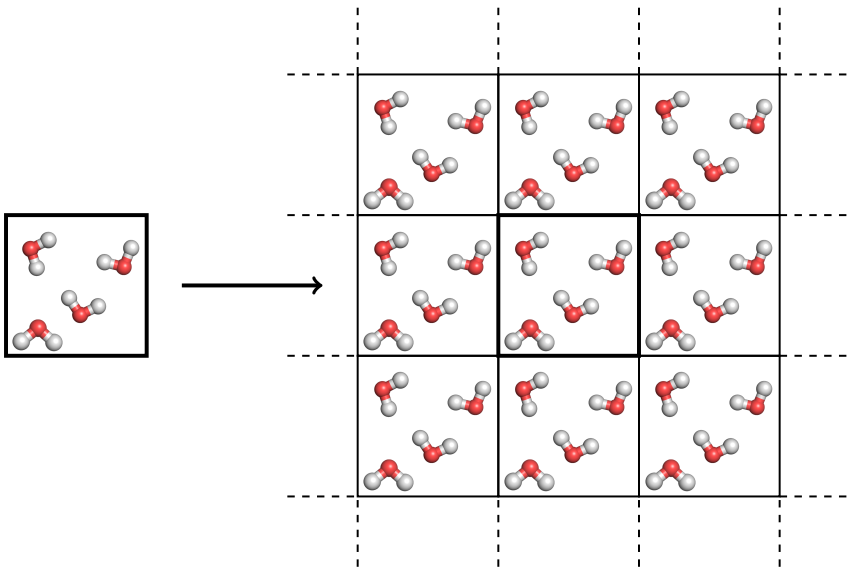

Figure 3.6 *Periodic boundary conditions in two dimensions [53].*

Periodic boundary conditions mean that after a molecule reaches a wall on one side of the box, it passes through back into the same box from the wall on opposite side. As visible from figure 3.6, the same simulation box is repeated in all directions, which practically imitates the simulation of an infinite system. This makes the use of PBC very attractive, because it is possible to achieve results corresponding to a huge system by using smaller system sizes, which means using less time and computational resources. It needs to be taken into account though that size of the system is not too small to allow the molecules to interact with copies of themselves. For example, a big polymer passing through a periodic boundary and back into the simulation box from the opposite side, could be in the reach of the long-range interactions discussed in section 3.2.2. This is avoided by the usage of sufficiently large systems and the previously mentioned cut-off radii for the non-bonded interactions, which can not exceed half the size of the shortest box vector. [6, p. 11–14][45, p. 141–145]

3.6 Thermostats and barostats

In addition to the structure of the molecules and to how they interact with each other, the conditions in which the simulation takes place also need to be defined. The volume of the system is given by the simulation box discussed in chapter 3.5, but simulation temperature and pressure are also required. They are set to be the same as in natural conditions or in experimental situations, such as the manufacturing process of the studied material. MD simulations are usually performed in either conditions where the number of particles N, the volume V and the temperature T stay constant (NVT), or in conditions where N, the pressure p and the temperature T stay constant (NPT) [6, p. 29–41]. It is also recommended to carry out short NVT and NPT simulations before the actual production MD simulation, to make sure that the system properly relaxes and adjusts to the desired simulation temperature and pressure [5].

It is often also desirable to make sure that the temperature and the pressure stay relatively constant during the simulation. This is achieved with the inclusion of temperature and pressure coupling algorithms, which are often called thermostats and barostats. Different thermostats such as Berendsen [54], velocity-rescale [55] and Nosé–Hoover -thermostats [56] exist, with Nosé–Hoover being the one used in this work. Options for the barostat include for example Berendsen [54], Parrinello–Rahman [57] and Martyna–Tuckerman–Tobias–Klein (MTTK) [58] barostat. In this work, the Parrinello–Rahman barostat was used. The different thermostats and barostats and their differences are discussed in more detail in reference [6, p. 29–41].

4. QUANTUM MECHANICS

The QM theory was developed to explain the structure of molecules theoretically, because many properties of molecules depend on their electronic structure. This is why determining the electronic structure of a studied molecule is often the ultimate goal in computational chemistry. It can be done by solving the Schrödinger equation, which can be used to calculate all properties of a molecular system. The equation gives an energy of the molecule as a function of its wave function. When the wave function is known, it can be used to determine many physical properties of the system such as bonding energies, excitation energies, and potential energy surfaces. Theories behind the QM methods used in this thesis are described briefly in this chapter without focusing too much on the mathematics. The equations shown here are presented in a simplified form, more detailed versions can be found from the references. [59, p. 295–296]

4.1 Schrödinger equation

The time-independent Schrödinger equation has a mathematical form of

$$\hat{H}\Psi(\mathbf{x},\mathbf{R}) = E_{TOT}\Psi(\mathbf{x},\mathbf{R}), \tag{4.1}$$

where Ψ is the wave function of the system consisting of M nuclei and N electrons, and $\mathbf{R} = \mathbf{R}_1, \mathbf{R}_2, ..., \mathbf{R}_M$ and $\mathbf{x} = \mathbf{x}_1, \mathbf{x}_2, ..., \mathbf{x}_N$ are sets of M nuclear and N electronic coordinates. E_{TOT} is the total energy and $\hat{H}$ is the Hamiltonian operator of the system [18, p. 307–308]. It has the form of

$$\hat{H} = \hat{T}_n(\mathbf{R}) + \hat{T}_e(\mathbf{x}) + \hat{V}_{nn}(\mathbf{R}) + \hat{V}_{ee}(\mathbf{x}) + \hat{V}_{en}(\mathbf{R},\mathbf{x}), \tag{4.2}$$

where $\hat{T}_n$ and $\hat{T}_e$ describe the kinetic energy of the nuclei and the electrons. The $\hat{V}_{nn}$ and $\hat{V}_{ee}$ represent the repulsive potential caused by nucleus-nucleus and electron-electron interactions, and $\hat{V}_{en}$ represents the attractive electrostatic interaction be-

tween the electrons and the nuclei. This equation defines the molecular system exactly. [60, p. 10–11]

It is however impossible to solve the Schrödinger equation analytically for even the simplest of molecules, because they consist of too many particles. This is because each nucleus and electron in the system has three coordinates, which for a system consisting of M nuclei and N electrons makes a total of $3(M + N)$ variables. [60, p. 10–11]

To simplify the equation, the Born-Oppenheimer approximation [59, p. 258] is adopted. It takes note of the great difference in mass between the electrons and the nuclei. Because of their larger mass, the nuclei move more slowly than the electrons, and it is possible to consider electrons moving in the field of the fixed nuclei. For the Hamiltonian operator in equation 4.2, this means that the kinetic energy of the nuclei is zero, and their potential energy is a constant. With the Born-Oppenheimer approximation, the electronic Hamiltonian operator is given by

$$\hat{H}_e = \hat{T}_e(\mathbf{x}) + \hat{V}_{ee}(\mathbf{x}) + \hat{V}_{en}(\mathbf{R}, \mathbf{x}), \tag{4.3}$$

which gives the Schrödinger equation the form of

$$\hat{H}_e \Psi_e(\mathbf{x}, \mathbf{R}) = E_e \Psi_e(\mathbf{x}, \mathbf{R}), \tag{4.4}$$

where Ψ_e is now the electronic wave function and E_e the electronic energy. The total energy E_{TOT} is given as a sum $E_{TOT} = E_e + E_n$ of this electronic energy E_e and the nuclear repulsion term $E_n = \hat{V}_{nn}(\mathbf{R})$, which in this approximation is a constant. [59, p. 258–260]

4.2 Density functional theory

The Schrödinger equation can be approximated either by wave function or DFT methods, with DFT being the dominant method of the two used in the field today. The basic idea behind the method was first proposed by L.H. Thomas [61] and E. Fermi [62] in 1927. They suggested a correspondence between the electron density of the molecule and its energy. This means that the electron density becomes the central quantity in DFT. [59, p. 239]

There are few advantages of using the electron density in the calculations. One of them being that instead of solving the wave function, which in reality does not exist, the method is based on a physical property that can be measured experimentally. Electron density can be observed whereas the wave function is only a mathematical construct, albeit an extremely useful one. Secondly, the electron density depends only on three spatial variables [60, p. 18]. It is not dependent on the number of electrons, so even with an increasing number of electrons, the electron density can be expressed by three coordinates only [63, p. 19]. This means that the calculations can be performed efficiently even for large molecules.

The equations and principles presented here are for the time-independent DFT, which determines ground state properties of molecular systems when the conditions stay static [63, p. 22]. The method performs well in these cases, but time-dependent situations, where the system and therefore the electron density varies with time, are out of reach for normal DFT. However these problems can also be tackled with an extension of the theory called time-dependent density functional theory (TD-DFT), but this is out of scope of this thesis, and is not discussed further.

4.2.1 Hohenberg–Kohn theorems

In 1964, Hohenberg and Kohn gave formal proof for the assumptions Thomas and Fermi had proposed in their work [64]. Hohenberg and Kohn described density functional theory in its present form and gave two theorems which form the basis of the method. The theorems are called Hohenberg–Kohn existence theorem and the Hohenberg–Kohn variational theorem. [59, p. 317–319]

The first theorem, the existence theorem, states that the ground state energy and all other ground-state electronic properties are uniquely determined by the electron density [59, p. 317]. This means that the ground state electron density is significant, because it determines the Hamiltonian operator and therefore all electronic states of the system [63, p. 19]. Mathematically this means that the ground state energy E_0 can be expressed as

$$E_0(\boldsymbol{\rho}) = \Big(T_e(\boldsymbol{\rho}) + V_{ee}(\boldsymbol{\rho})\Big) + V_{en}(\boldsymbol{\rho}) = F_{HK}(\boldsymbol{\rho}) + V_{en}(\boldsymbol{\rho}), \tag{4.5}$$

where V_{en} is again the attractive electrostatic interaction between the electrons and the nuclei and the sum of the kinetic energy term of the electrons T_e and repulsive potential energy term between the electrons V_{ee} form a new functional F_{HK}, the

Hohenberg–Kohn functional. All other terms in the equation 4.5 are also functionals of the electron density $\boldsymbol{\rho}$. [60, p. 19]

The exact form of the F_{HK} is not known, and finding it is the main challenge in the DFT. If it were known, the Schrödinger equation could be solved completely. F_{HK} is a universally valid functional, its form doesn not depend on the system, so it applies the same to a hydrogen atom as to huge molecules such as polymers. [63, p. 20]

The first theorem states that the ground state electron density is sufficient for obtaining all properties of an electronic system, but it does not say anything about how to identify the ground state density [63, p. 20]. The second Hohenberg–Kohn theorem, the variational theorem, states that the functional that delivers the ground state energy of the system, delivers the lowest energy only if the input density is the true ground state density. [59, p. 319]

4.2.2 Kohn–Sham approach

The next major step for solving the form of F_{HK} functional came in 1965 by Kohn and Sham [65]. They suggested calculating the exact kinetic energy of the system consisting of non-interacting electrons with the same electron density as the real system with interacting electrons. Their theory describes mathematics and correlations between electron densities and molecular energies [66, p. 20–22]. Based on their work, the ground state energy of a molecule in its simplest form is given by

$$E_0(\boldsymbol{\rho}) = T_e(\boldsymbol{\rho}) + V_{ee}(\boldsymbol{\rho}) + V_{en}(\boldsymbol{\rho}) + E_{xc}(\boldsymbol{\rho}), \tag{4.6}$$

where the first three terms are the same as in equation 4.5, and E_{xc} is functional called the electron-electron exchange-correlation energy. This is a functional which contains everything that is not known of the system, while the first three functionals in equation 4.6 can be determined. Again, if the form of E_{xc} were known, the Schrödinger equation could be solved exactly. Until that is the case, different approximations for it must be used. [63, p. 21]

Currently there are three main types of approximations for the exchange-correlation functional E_{xc}. The local density approximation (LDA) is based on the idea of a uniform electron gas, which assumes that the electron density is uniform throughout the molecule. This is not the case in real molecules, where the electron density is far

from homogenous. Methods which take this into account note that the exchange-correlation energy depends not only on the electron density but also on electron density gradient. This is called the generalized gradient approximation (GGA). The most popular ones in use today are called global hybrid methods, and they mix together a fixed, global fraction of explicit Hartree–Fock (HF) exchange [59, p. 295–298][67] and the DFT exchange-correlation energy.

The long-range corrected (LRC) functional ωB97XD [68], which includes empirical dispersion, was the one used in the calculations carried out on this thesis (default value for the range separation parameter ω of 0.20 bohr^{-1} was used). This LRC functional has also been used in other studies of PSCs [10][11][44], and it is recommended to use a LRC functional for the constrained geometry optimizations required for the parametrization of the torsional force field parameters, to generate accurate torsion barries and local minima [5].

4.3 Basis sets

Lastly the solving of electronic structure requires the selection of a basis set. Basis sets are a set of one-particle mathematical functions that represent atomic orbitals (AOs), from which molecular orbitals are being built from. Several different ways of representing the AOs exist, but the most widely used ones are Gaussian-type orbitals (GTOs). For more accurate results, they are often used as a linear combination of many GTOs, which is called a contracted GTO (CGTO). [59, p. 302–307][60, p. 29–31]

The simplest type of a basis set would apply only one basis function, which could be either a GTO or CGTO, for each atomic orbital in the atom. These are called minimal basis sets. They are suitable for calculations involving atoms, but for molecules, so called double-zeta basis sets are of often used. They apply two basis functions for each AO. There are also split–valence basis sets, which use one basis function for each core orbital, and more basis functions for the valence orbitals. The aim is to treat the valence orbitals with more accuracy than the core orbitals, because the changes in chemical processes occur in the valence orbitals, with the core states staying relatively the same. [60, p. 29–31]

Other additional functions are often included to the basis sets to improve their description of real molecules. These are for example polarization functions, which describe the polarization of the AOs. This happens when other atoms approach the orbitals, which causes them to shift one way or the other. Another addition

would be the inclusion of diffuse functions, which hold the electron in the orbital far from the nucleus. They are necessary for example for the description of very electronegative atoms and van der Waals complexes. [59, p. 302–307][60, p. 29–31]

The basis set used in the DFT calculations carried out on this thesis was Pople's basis set 6–31G** or 6–31G(d,p) [69]. This is a split–valence double–zeta basis set, where the core orbital is a CGTO made of six GTOs. Valence orbitals are described by two orbitals, one of which is a CGTO made of three GTOs, and the other a single GTO. The asterixs at the end denote that polarization functions added to both the heavy atoms and hydrogen, respectively. The polarization of the heavy atoms is taken into account with d-orbitals and of the hydrogens with p-orbitals. This basis set was chosen because it has been used in other studies where the force field was parametrized for the studied PSC molecule [10][11][44].

5. MODELS AND METHODS

This chapter deals with the computations and simulations carried out in this thesis. The section 5.1 explains how the force field was parametrized for the studied BDT-TPD polymer. Section 5.2 outlines on what types of systems the force field was applied to, and section 5.3 focuses on how the simulations were conducted. The results of these simulations and their significance is discussed later in chapter 6.

5.1 Parametrization of a force field

The OPLS-AA is a very commonly used force field in MD simulations. However it has been developed mostly for simulations of organic biomolecules in water [7]. It performs well in these cases, because the force field contains all the required parameters to describe the structures found in biomolecules, such as nucleic acids and amino acids. It is not designed for simulations of conjugated polymers that are used in PSCs, which means some adjustments need to be made in these situations. In this work OPLS-AA has been used as a template for building the force field for the simulations, but to achieve a better accuracy for the studied BDT-TPD polymer, it has been parametrized against the results of the DFT calculations, and certain parameters in the force field have been adjusted to better describe the atoms and their interactions in the PBDT-TPD.

5.1.1 Defining the structure of the repeating unit

The structure of a repeating unit of PBDT-TPD, which is shown in figure 5.1, was built with Avogadro software [70][71]. Side-chains for the polymer were chosen to be 2-ethylhexyls for BDTs and heptyls for TPDs, because these side-chains were noted to yield the best performance in reference [72]. The initial coordinates for each atom were therefore acquired from the Avogadro software. Atoms in the monomer were each given a unique atom name, which are shown in figures 5.2 and 5.3. The next step was to define the properties of the atoms by dividing them into different atom types, according to principles explained in section 3.1.

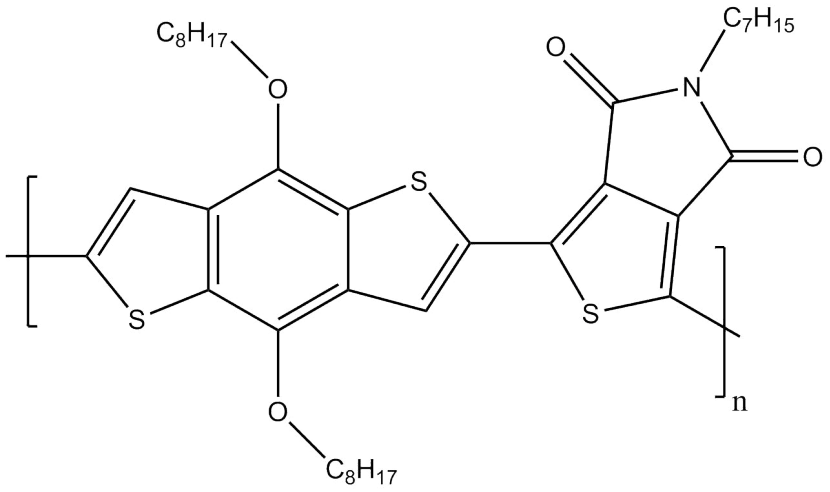

Figure 5.1 *Structural formula of the repeating unit of the PBDT-TPD polymer. Sidechains, 2-ethylhexyl (C_8H_{17}) and heptyl (C_7H_{15}), are not shown for clarity.*

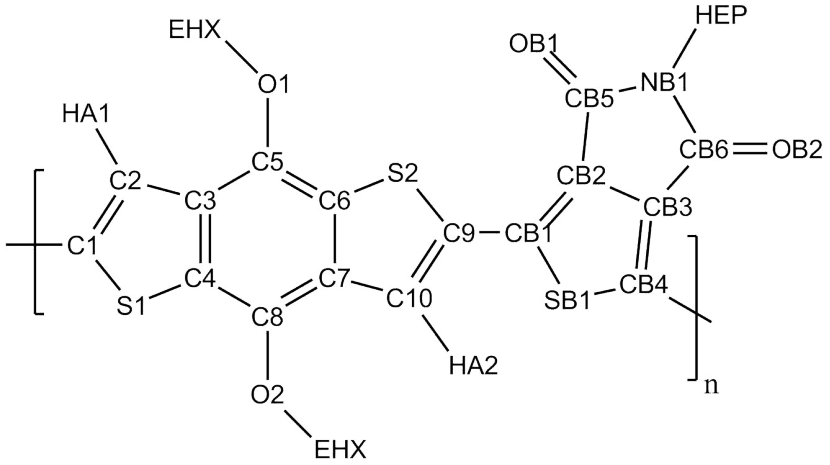

Figure 5.2 *Atom names used for the repeating unit of the PBDT-TPD polymer. Atom names in the side chains, written here by their residue names, are shown below.*

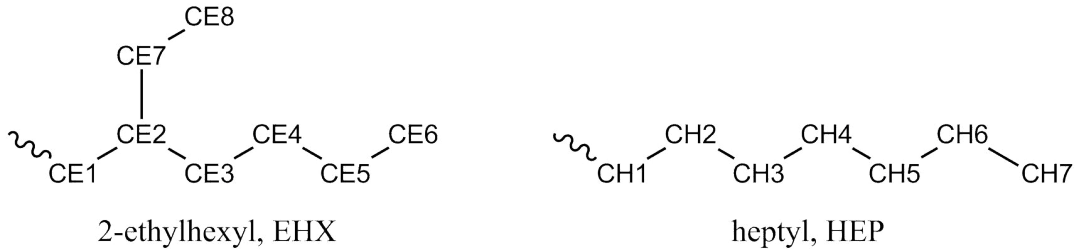

Figure 5.3 *Atom names used for the 2-ethylhexyl and heptyl side chains. Hydrogens attached to the carbon atoms are not shown for clarity, but they are named accordingly (see text for more information).*

As visible from figure 5.2, the atoms in the BDT moiety have been mostly named after their element and a sequential number. This is the case also for the TPD moiety, but there the atoms also have a letter B in their name to differentiate them from the BDT atom names. The atom names of the side chains are shown in figure 5.3, and all the carbons in the 2-ethylhexyls have a name CE with a sequential number, and in heptyls a name CH with a sequential number. All hydrogen atoms in the side chains have a name that is related to the carbon atom they are attached to, and a letter A, B or C to differentiate hydrogens that are attached to the same carbon from each other. For example, hydrogens connected to the 2-ethylhexyl carbon CE6 have the names HE6A, HE6B and HE6C, and hydrogens attached to heptyl carbon CH2 have the names HC2A and HC2B.

For building the force field and for defining the different atom types in the polymer, the OPLS-AA force field [7] was used as a template. The atom types were acquired as a combination from different types of molecules, that have in structural parts similar to those in the repeating unit of the PBDT-TPD polymer. These different types of molecules from where the atom types were taken are shown in figure 5.4.

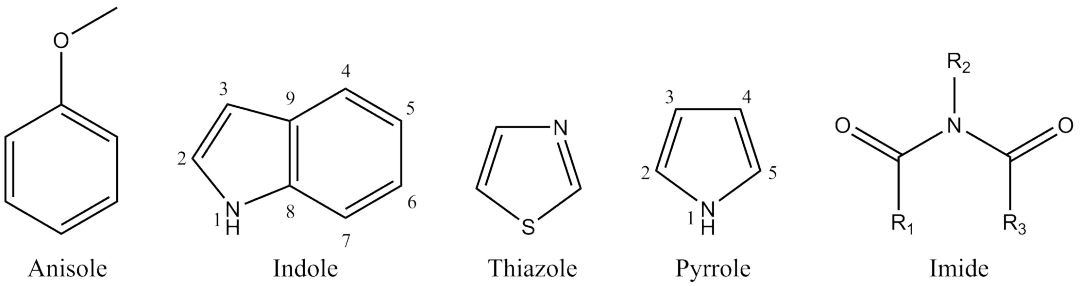

Figure 5.4 *Different types of molecules that were used in acquiring the OPLS-AA force field parameters for the repeating unit of the PBDT-TPD polymer. Heavy atoms in indole and pyrrole are numbered for the purpose of table 5.1.*

The atom types for the benzo ring in BDT were taken from anisole and indole. The OPLS-AA force field does not contain parameters for a thiophene molecule, which is a five-membered heterocyclic compound containing sulphur. Therefore parameters for the sulphur atom have been taken from thiazole, and those for the carbon atoms in the 5-membered thiophene rings in both BDT and TPD from indole and pyrrole. For the 5-membered nitrogen ring in TPD, the atom types of an imide structure have been used. Sometimes the atom types were given different names from those in the OPLS-AA to give a more accurate description of the structure of PBDT-TPD specifically. Final atom types in the modified force field are presented in figure 5.5 and in table 5.1.

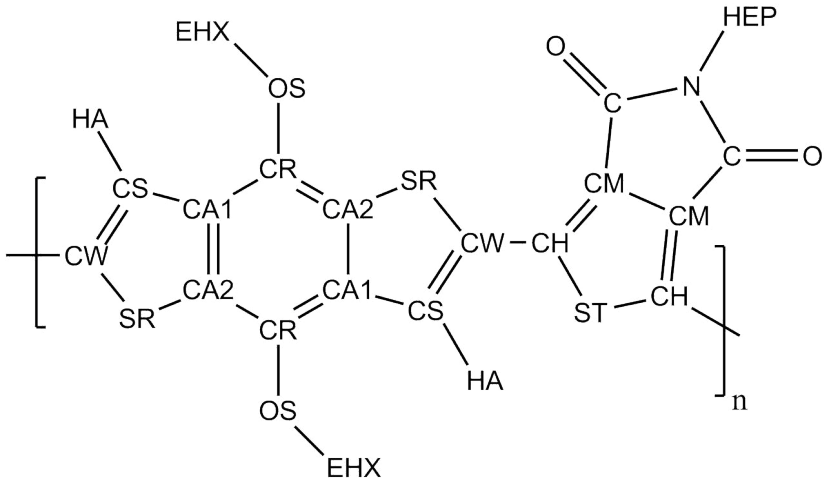

Figure 5.5 *Final atom types used in the repeating unit of the PBDT-TPD polymer.*

Table 5.1 *OPLS-AA numbers and atom types corresponding to the new atom types in the modified OPLS-AA style force field, and the basis corresponding to the origin of each atom type in the molecules presented in figure 5.4.*

new atom type	**OPLS number**	**OPLS atom type**	**basis**
SR	opls_633	S	S in thiazole
CW	opls_543	CW	C2 in pyrrole
CS	opls_544	CS	C3 in pyrrole
CA1	opls_595	CB	C9 in indole
CA2	opls_594	CN	C8 in indole
CR	opls_590	CA	C4 in indole
OS	opls_179	OS	O in anisole
HA	opls_546	HA	H3 in pyrrole
ST	opls_633	S	S in thiazole
CH	opls_543	CW	C2 in pyrrole
CM	opls_544	CS	C3 in pyrrole
C	opls_252	C	C(=O) in imide
N	opls_251	N	N in imide
O	opls_253	O	O in imide
HC	opls_140	HC	alkane H
CE	opls_135, 136, 137	CT	alkane C
CT	opls_135, 136	CT	alkane C

Atom types for the side chains are not shown for clarity in picture 5.2, but in the modified force field every carbon atom in 2-ethylhexyl has an atom type of CE, and every carbon atom in heptyl has an atom type of CT. All hydrogens in both of the side chains have an atom type of HC. Parameters for the atom types in the side chains were acquired from the OPLS-AA parameters for alkane carbon and alkane hydrogen. It is shown in table 5.1, that the atom types CE and CT of the side chains have a few different OPLS numbers. This is based on how many alkane hydrogens are bonded to the carbon atom. This difference does not influence the bonded parameters and only affects the partial charges of these alkane carbons, where they have been taken into account in the modified force field.

As presented in figure 5.5, the BDT and TPD moieties in the polymer are thought to be symmetrical which means that atom at one side of the molecule will have the same atom type as the similar atom at the opposite side of the molecule. For example, in BDT atoms C2 and C10 both have the same atom type CS. The atom types also have been defined so that there is no same atom type in both BDT and TPD. This is done to more accurately define different types of bonds, angles and dihedrals in the molecule.

5.1.2 Bonded and non-bonded force field parameters

The DFT calculations were performed to make a tailor-made force field for the polymer simulations, and the ground-state optimization was performed using the Gaussian 09 software [8] with the ωB97XD LRC functional [68] and the Pople's basis set 6–31G** [69]. The structure optimized was a BDT-TPD trimer with side chains. Trimer was chosen to take into account the effect of the head and tail of the polymer. At both ends the atoms are not in such a crowded environment as in the middle part of the polymer, which affects the bonded parameters of the molecule, such as bond lengths and angles, and also the partial charges of different atoms. Therefore these parameters were taken from the middle part of the trimer of the optimized structure, to mimic more accurately the possible structure of the infinite polymer, and to avoid the chain end effects present in the side repeating units of the finite oligomer [73]. Usually the parametrizations have been done for smaller structures such as monomers [10][13], but the end effects in these cases might not be taken into account as well as they are with bigger structures. The next paragraphs outline where the different parameters were acquired from and how they were adjusted. A complete list of all the parameters in the modified force field can be found in the appendix A. [5]

Bonds between two atom types are described according to equation 3.5. The two parameters needed are the force constants k_{ij}^{b} and the reference bond lengths b_{ij}^{0}. Force constants were obtained directly from the OPLS-AA force field, for the atom types in the molecules shown in figure 5.4. The bond lengths were taken from the optimized trimer structure as an average values from the middle repeating unit of the trimer with the side chains. As for the side chains, both the force constant and bond length values were obtained from the OPLS-AA force field.

Angles between three atom types are described by equation 3.6, and the two required parameters are the angular force constants k_{ijk}^{θ} and the reference angles θ_{ijk}^{0}. Similarly to the bond lengths, the angular force constants were again taken from the OPLS-AA force field, and angles as average values from the optimized structure of the middle repeating unit of the trimer with the side chains. They were also modified a bit so that the sum of the angles in the 5-membered rings is 540 degrees, and in the benzene ring 720 degrees, which are the sums of interior angles in a pentagon and a hexagon, respectively. It was also checked that the sum of the three angles for all atoms that are in the same plane and connected by a same carbon atom is 360 degrees. For example in figure 5.5, looking at atom type CA1, the sum of the three angles (CR-CA1-CA2, CR-CA1-CS, CS-CA1-CA2) should be 360 degrees. This was done to avoid the angle values from unnecessarily twitching the atoms out of plane. In the case of the side chains, these values were again taken directly from the OPLS-AA force field.

Proper dihedrals are described by the Ryckaert–Bellemans function shown in equation 3.8, which has six coefficients C_0–C_5 that need to be defined for the four atom types in the dihedral. These were all taken from the OPLS-AA force field, but new coefficients for the dihedral between BDT and TPD (SR-CW-CH-ST in figure 5.5) were parameterized with reference to the DFT results. This dihedral determines the conformation of the polymer backbone and it is therefore important to obtain accurate parameters for it [5][13][39]. It should first be noted though that the scans here were performed for a trimer with methyls as the side chains, as the geometries of some of the trimer conformers with the 2-ethylhexyls and heptyl side chains did not converge in the DFT calculations. The longer side chains also induced too many degrees of freedom to the potential energy curve of the studied dihedral, complicating the following steps in the method. The method for parametrizing the RB coefficients is illustrated in a flow chart in figure 5.6, and the different steps are explained in the following paragraphs. The same process is also explained in the supporting information of reference [74].

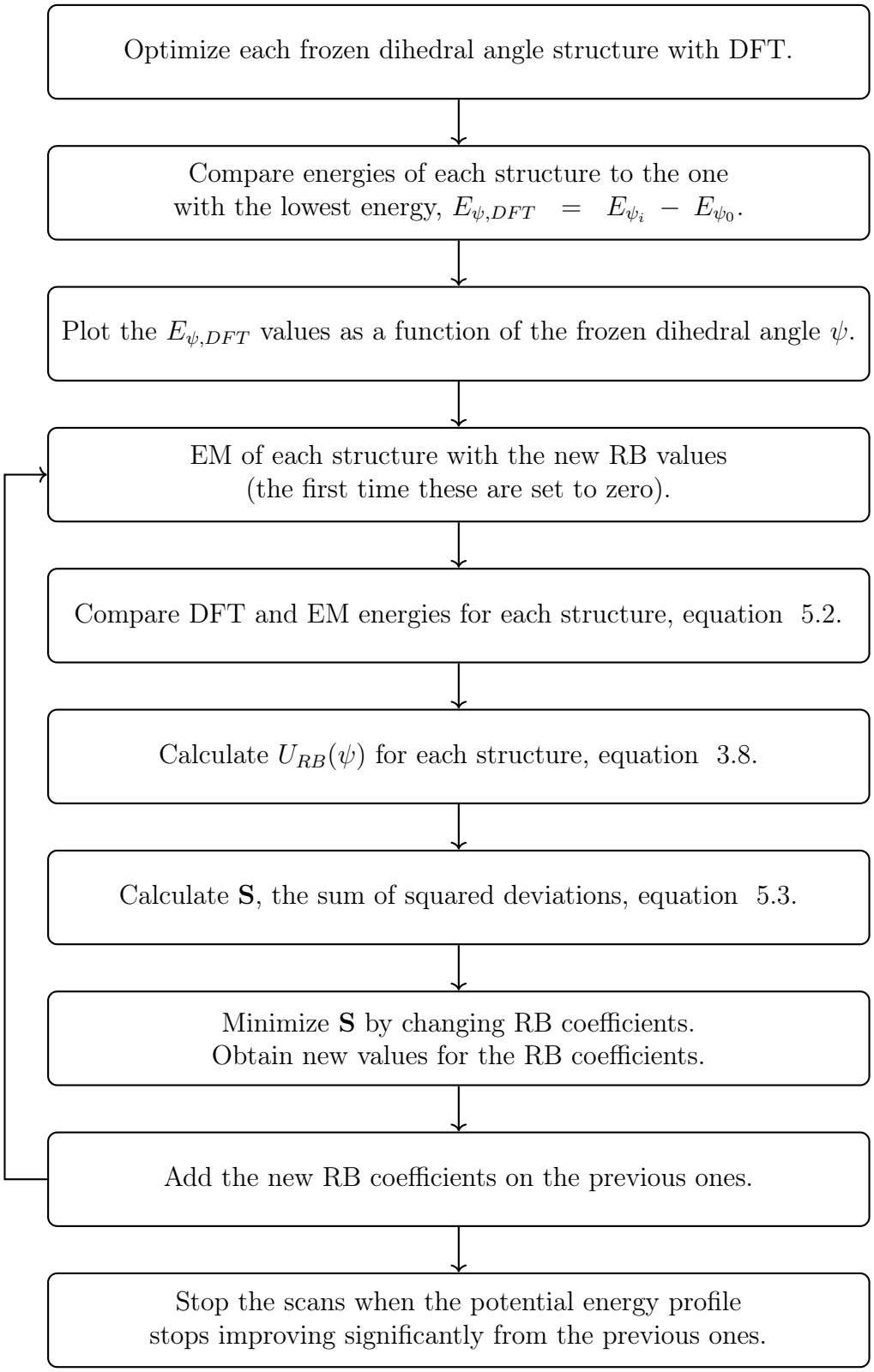

Figure 5.6 *The steps taken in parametrizing RB coefficients for the ST-CW-CH-ST dihedral between BDT and TPD. Each step is explained in more detail in the text.*

The calculations were done by freezing the middle dihedral angle of the trimer into certain conformation using dihedral restraints, and then optimizing the geometry of this trimer with DFT. These restrained geometry optimizations were performed at five degree intervals. This means that while the studied dihedral angle was frozen, the geometry of the trimer was otherwise fully optimized at the ωB97XD/6–31G** level of theory. The total energies of each frozen dihedral angle structure E_{ψ_i} were compared to the structure with the lowest energy E_{ψ_0},

$$E_{\psi,DFT} = E_{\psi_i} - E_{\psi_0}. \tag{5.1}$$

These potential energy values relative to the lowest energy for each dihedral angle value $E_{\psi,DFT}$ were plotted as a function of the frozen dihedral angle ψ. The resulting potential energy profile is presented in figure 5.7.

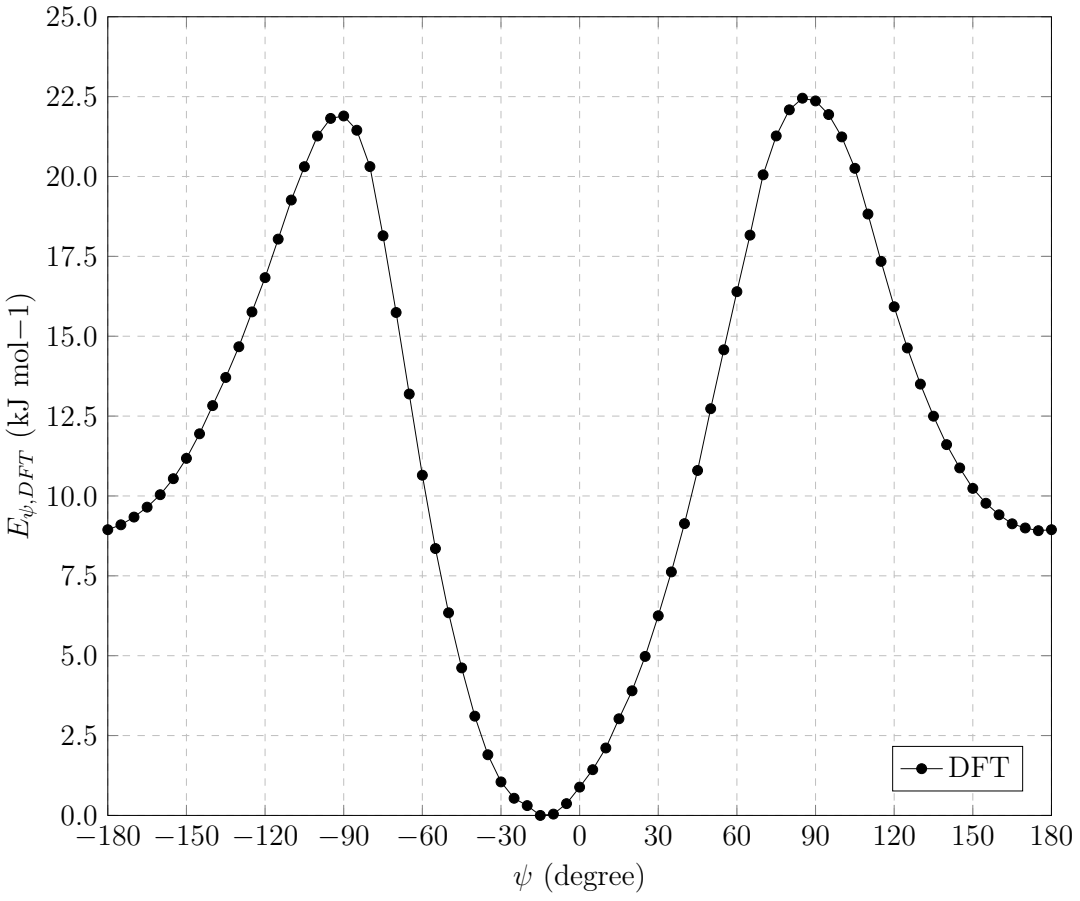

Figure 5.7 *Profile of the DFT potential energy $E_{\psi,DFT}$ as a function of the frozen dihedral angle ψ.*

As visible from the figure 5.7, the lowest potential energy for the trimer is in this case acquired when the middle dihedral angle has the value of $\psi = -15°$. This corresponds to so-called *syn*-conformation of the BDT-TPD polymer, where the sulphur atoms in both BDT and TPD are on the same side of the polymer backbone, and on a slight 15° angle from each other.

The six RB coefficients for the studied dihedral were set to zero in the beginning of the EM calculations. After this, EM calculations were performed on the same frozen dihedral angle trimer structures as in DFT. The DFT optimized geometries were used as input structures for these corresponding restrained geometry optimizations with EM, and the energies of these $E_{\psi,EM}$ were compared with reference to those of the DFT calculations.

$$\Delta E_\psi = E_{\psi,DFT} - E_{\psi,EM} \tag{5.2}$$

The idea of this method is that with the ideal coefficients for the dihedral angle, the MD calculations should produce the same potential energy profile as the DFT calculations. Thus, in an ideal case the difference between the energies ΔE_ψ with each dihedral angle should be zero. This is not the case yet, and the difference between the two energies is caused by the EM calculation not yet containing the ideal coefficients for the dihedral angle in the force field.

To account for the significance of the studied dihedral angle potential to the energy difference ΔE_ψ, next the RB potential energy is calculated by equation 3.8 for each frozen dihedral angle value. This energy for the dihedral angle $U_{RB}(\psi)$ is compared to the energy difference ΔE_ψ, and the sum of the squared deviations $\mathbf{S}$ of the two is calculated by equation

$$\mathbf{S} = \sum_{\psi=-180°}^{180°} (\Delta E_\psi - U_{RB}(\psi))^2, \tag{5.3}$$

where the angle ψ is in five degree intervals. The value of the summation is then minimized by changing the six RB coefficients in equation 3.8. The parameters that obtain the lowest possible value for the sum of the squared deviations in equation 5.3, are the RB coefficients for the fit, and they are added as a summation on top of the previous values, which in the beginning were set to zero.

This process is repeated a few times, which is shown as the loop in figure 5.6. With the force field updated for the new RB coefficients acquired from the EM scan, new energy minimization calculations are performed for each frozen dihedral angle structure, and their energies are again compared to those of the DFT calculations. New fits for the RB coefficients are obtained, which are then added to the previous RB values and the loop is started again. After each completed loop the energies from the EM calculations converge a bit closer to the DFT values, but after a few rounds there is no longer significant improvement over the previous values. This was noted to happen in the scans after five loops, which means that further calculations were not necessary, and values for the dihedral were obtained from the fifth fit for the RB function. The potential energy profiles of these five EM scans are shown in figure 5.8.

As visible from the figure 5.8, the first EM potential energy profile 5.8(a) is quite far from the DFT energy profile. The second scan 5.8(b) improves the EM profile and converges it closer to the shape of the DFT profile, but there are still quite many variations. The subsequent scans 5.8(c) and 5.8(d) already produce an energy profile that converges closer to the DFT energy profile than the previous steps, with the final scan 5.8(e) being the step after which scans were stopped, as mentioned previously.

The small variations in the EM scans, most noticeable in figures 5.8(c)–5.8(e) around the $\psi = 0$–$30°$ dihedral angle, are caused by the differences in the calculation methods between EM and DFT. The algorithms do not necessarily find the global energy minimum for the structure, but find quite easily the local energy minimum. Therefore, local energy minimum found by one method may not be the same as the local energy minimum found by the other method. Nevertheless, after five loops the acquired EM potential energy profile already follows the shape and the energy values of the DFT energy profile closely 5.8(e), with the single biggest energy difference between the profiles being 3.0 kJ mol^{-1} at $\psi = 5°$. The close resemblance of the energy profiles means that RB coefficients for the force field were acquired from this scan, and these RB coefficients used in the final modified OPLS-AA force field are shown in table 5.2.

Table 5.2 *The parametrized Ryckaert–Bellemans dihedral values for the SR-CW-CH-ST dihedral optimized for the modified OPLS-AA force field in this work.*

C_0	C_1	C_2	C_3	C_4	C_5
29.49537	7.77359	-31.40990	2.43505	6.46315	-0.06355

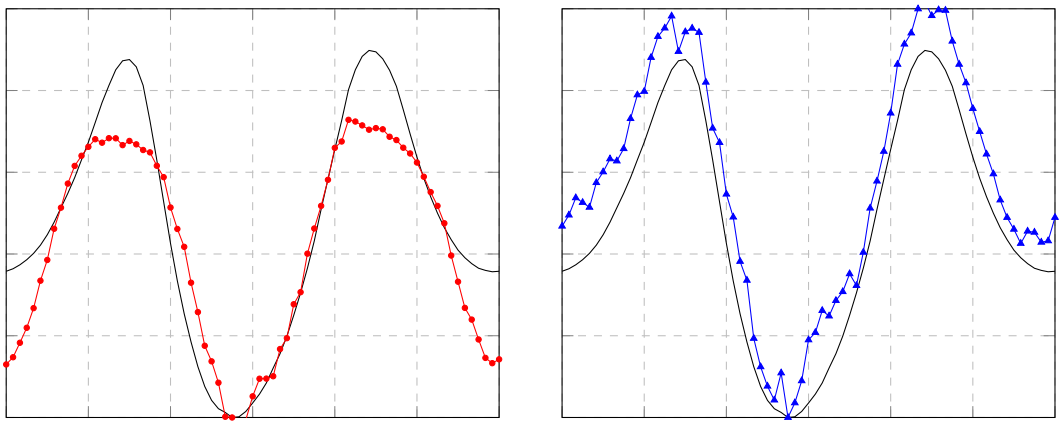

(a) EM scan 1

(b) EM scan 2

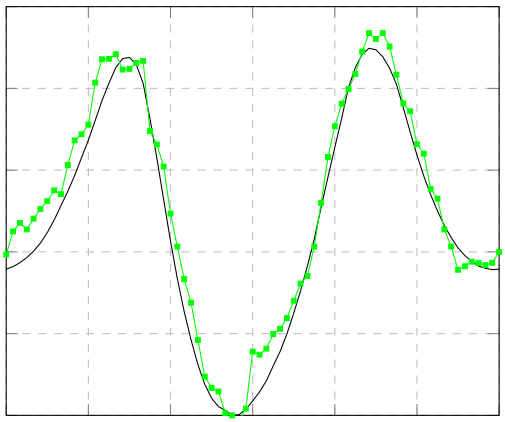

(c) EM scan 3

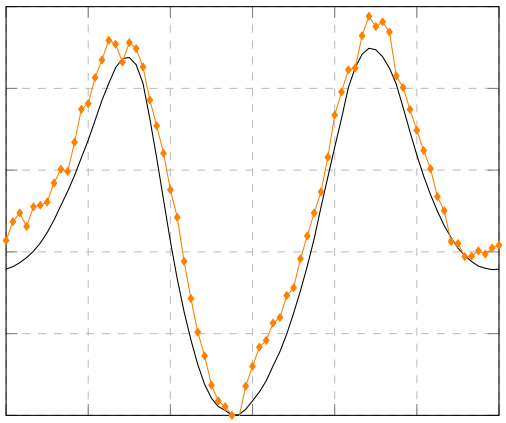

(d) EM scan 4

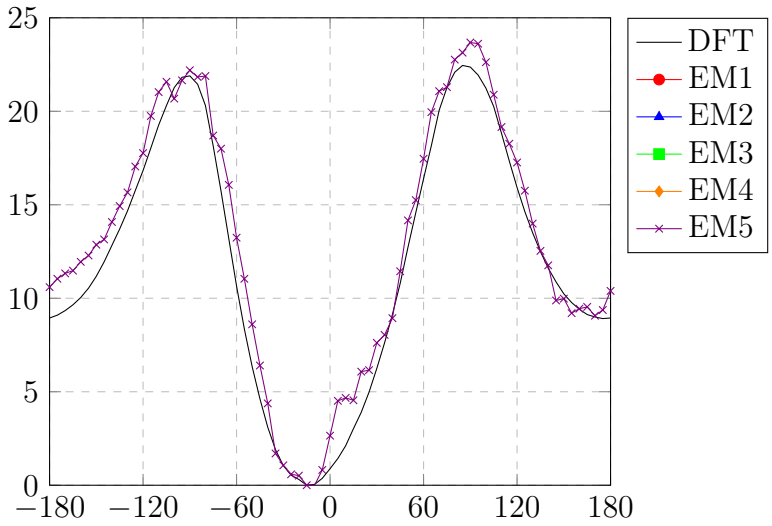

(e) EM scan 5

Figure 5.8 *The potential energy profiles of five different subsequent EM scans (a) - (e) compared to the potential energy profile of the DFT calculation. All figures have the same axis scale as figure (e) and in each figure the DFT scan is the same. All x-axes have the units of degree for the frozen dihedral angle ψ and y-axes kJ mol−1 for energy. Figure (e) shows the potential energy profile with the RB coefficients in table 5.2, which were the ones used in the final modified force field.*

Improper dihedrals are represented by equation 3.10 and their function is to keep the four atom types defined in it planar. The values required here are the force constants k^{ξ}_{ijkl} and the reference values for the dihedral angle ξ^{0}_{ijkl}. The OPLS-AA force field currently defines all improper dihedrals through Ryckaert–Bellemans dihedrals, but the harmonic type dihedral used here is also compatible with it. In this function type the reference angle has always the value of zero, and the force constant is k^{ξ}_{ijkl} is 167.400 kJ mol^{-1} rad^{-2}, which is a carryover from GROMOS force field [48].

As for the non-bonded interactions, to calculate the **Coulomb interaction**, described by equation 3.12, the partial charge of each atom is needed. These were taken from the middle repeating unit of the optimized trimer with the side chains. The charges were derived from the electrostatic potential by Merz–Singh–Kollman (MK) [75][76] method, and these MK charges for the BDT and TPD units were directly used. Partial charges for the side chains were taken from the OPLS-AA force field, but the charge of the first carbon atom of the side chains connected to the polymer backbone was modified a bit to ensure zero net charge for the repeating unit of the PBDT-TPD.

The final parameters needed are for the **Lennard–Jones interaction**, which is described by equation 3.13, and the required constants for all the different atom types used are the ϵ and σ parameters. Both of these were taken from the OPLS-AA force field for the atom types in the structures presented in figure 5.4.

5.2 Simulated systems

To test how the new modified force field performs in MD simulations, it was used on simulating four different types of PBDT-TPD systems as follows:

- One *anti*-conformation octamer in chloroform solvent.
- Six octamers with an *anti*-conformation in the crystalline phase in vacuum.
- Six octamers with a *syn*-conformation in the crystalline phase in vacuum.
- Six *anti*-conformation octamers in an amorphous phase in vacuum.

The modified force field was identical in all cases, except for the simulation in solvent, where the OPLS-AA [7] force field parameters for chloroform and equilibrium liquid

box structure consisting of 1000 chloroform molecules, as provided in reference [77], were used [78][79]. The simulations of the crystalline and amorphous phases were performed in vacuum.

In the simulations of the crystalline phases, the six octamers were initially placed in two rows next to each other with both rows having a stack of three chains on top of one another. In the first crystalline starting configuration, the initial conformation for the polymer chains was the *anti*-conformation, which means the neighbouring sulphur atoms in BDT and TPD moieties are not on the same side of the polymer backbone. This corresponds to the structural formula shown previously in the figure 5.1. In the second crystalline starting configuration, the chains were initially in the *syn*-conformation, with the neighbouring BDT and TPD sulphurs being on the same side of the polymer backbone. The starting configuration of the *syn*-conformation crystalline structure is visible from figure 5.9. To simulate an amorphous phase, the six octamers were initially placed in random positions close to each other. In the starting configuration for the amorphous system the chains were initially in the *anti*-conformation, as is visible from figure 5.10. Both of the mentioned figures have been made with the VMD software [80] using the tachyon render [81].

In addition to these simulations, we also tried to simulate bigger systems that consisted of 18 PBDT-TPD chains with 15 CRUs in both amorphous and crystalline phases, but these proved to be quite problematic to accomplish. This is because these systems already consist of over 25 000 atoms, which means they need to be

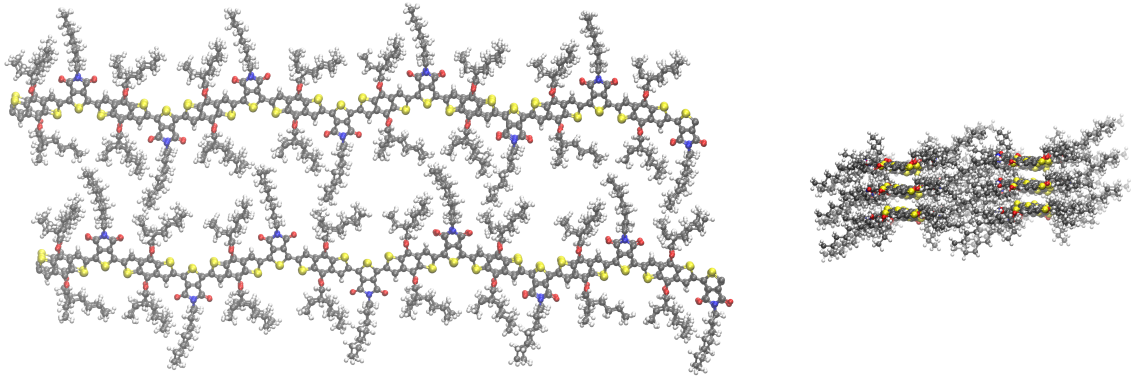

Figure 5.9 *Starting structure of the six 8mer PBDT-TPD polymers for the simulation of the syn-conformation crystalline structure illustrated from the top and from the side. Carbon atoms are colored gray, hydrogens white, oxygens red, nitrogen blue and sulphur yellow. The structure of the anti-conformation version is the same, but the sulphurs of BDTs and TPDs are on the same sides of the polymer backbone.*

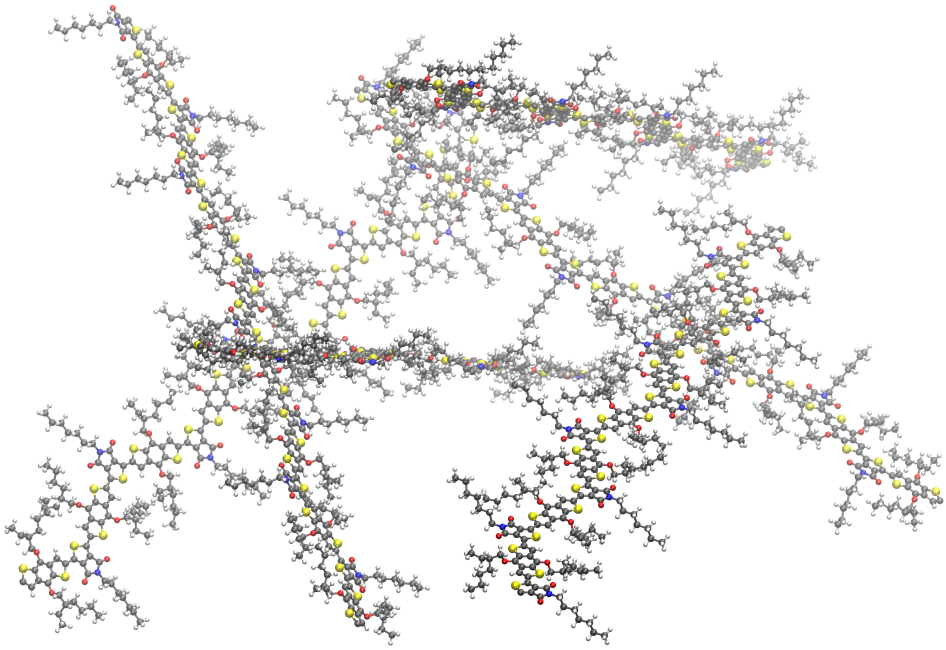

Figure 5.10 *Starting structure of the six 8mer PBDT-TPD polymers for the simulation of the amorphous structure. The different polymer chains are close to each other in a random configuration. Coloring scheme is the same as in figure 5.9.*

simulated in parallel [6, p. 56]. A short explanation of what this means is that the simulation box of the system is divided into smaller boxes by a grid called the domain decomposition grid. Then most of the computer cores that are allocated for the simulation are assigned to calculate potentials of atoms within one of these smaller boxes, with some cores being responsible for calculating the non-bonded potentials between atoms that interact from one small box to another. Each core does its calculations simultaneously with other cores, which massively shortens the simulation times in big systems. [6, p. 56–62]

However, this causes a problem in vacuum, because these types of systems include a lot of empty space. This means that because atoms are not distributed equally to all locations in the simulation box, in parallel simulations some cores might be allocated by the grid to do calculations for a smaller box that contains basically no atoms at all, while other cores are responsible for doing all the calculation work. This unbalance often causes a failure in the simulation. A workaround for this problem is to allocate less cores in total for the simulation, which makes the domain decomposition grid smaller, which in turn makes it more likely that each of the small boxes will contain some atoms, and all the cores are doing work in the calculation. By using less cores it was possible to calculate NVT-simulations for these systems,

but the next problem arises in the NPT-simulation. Because of the amount of empty vacuum space, the simulation box was noted to shrink an unnaturally large amount, which causes the behaviour of the molecules and the results of the NPT-simulations to not be sensible.

To avoid these problems in the future, the goal would be to minimize the empty vacuum space and fill the simulation box completely with polymers. One possible approach to achieve this would be to decrease the degree of polymerization of the polymer, but significantly increase the number of individual polymer chains in the system. Shorter polymer chains would make it easier to fill the empty spaces inside the simulation box, and the size of the simulation box can in the case of shorter polymer chains be smaller in general, to avoid the problem of polymer chains interacting with themselves as discussed in section 3.5. Unlike the vacuum simulations performed in this thesis, these type of simulations would mimic the structure of an infinite amorphous or crystalline phase of the polymer in the active layer, and they could be simulated in NPT conditions and with PBC, which has been the case in other studies as well [10][11][44].

5.3 Simulation parameters and algorithms

The systems were first energy minimized with the steepest descent algorithm explored in section 3.3 for 50 000 steps, or until the maximum force reached a value lower than 10 kJ mol^{-1} nm^{-1}. After this a NVT simulation of 2.5 ns was performed in order to relax the systems to the temperature of 300 K. For the vacuum systems, the production MD simulations were performed next, but for the solvent system, a NPT simulation of 2.5 ns was carried out to relax the system into the pressure of 1 bar. The systems were simulated for 5 ns in the final production MD simulations. A time step of 1.0 fs was used in all cases. The workflow of different simulations is presented as a flowchart in figure 5.11.

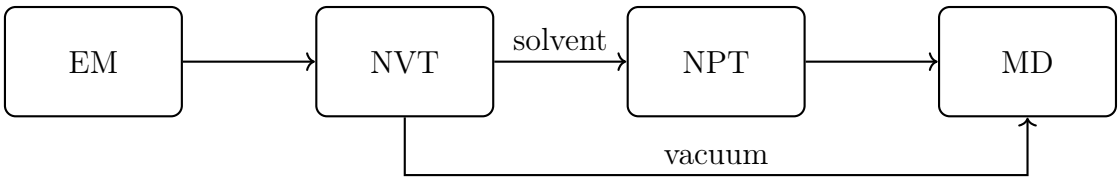

Figure 5.11 *The workflow of different simulations before the production MD simulations.*

In the **solvent simulation**, the center of mass translation was removed. The PBC were applied to a cubic simulation box with the length of all the box vectors being 11.5 nm, and the Verlet cut-off scheme [6, p. 19–20] was used. With the long range interactions, particle-particle particle-mesh algorithm (P3M-AD) [6, p. 107][82, p. 22–23] with a cut-off distance of 1.2 nm was used to calculate Coulomb electrostatics, and for the Van der Waals interactions a dispersion correction [6, p. 107–108] was applied, with the cut-off at 1.2 nm distance. The Nose–Hoover thermostat [56] with a time constant of 0.1 ps and a simulation temperature of 300 K was used for temperature coupling, with separate heat baths provided for the polymer and the chloroform solvent [6, p. 31–34]. The Parrinello–Rahman barostat [57] with isotropic scaling, time constant of 1.0 ps and simulation pressure of 1 bar was used for pressure coupling [6, p. 36–37]. The compressibility of chloroform (9.96×10^{-5} bar^{-1}) was acquired from reference [83].

In the **vacuum simulations**, both the center of mass translation and rotation around the center of mass were removed. As explained in section 3.5, PBC were not applied for the vacuum systems, and the simulation box was excessively large to avoid the effect of artificial walls in the simulations. This means that the group scheme with each atom in the system having its own group was used [6, p. 19–20]. Both the Coulomb and Van der Waals interactions were calculated without cut-off distances, which means that for each atom the long range interactions are calculated between all other atoms in the system. The parameters for the temperature coupling were identical to those used in the solvent simulations, and as illustrated by flowchart in figure 5.11, NPT simulations were not carried out for the vacuum systems.

All the simulations were performed with GROMACS version 5.1.2 [6] in the Taito cluster of the Center for Scientific Computing (CSC) – IT Center for Science, using the modified OPLS-AA -based force field made in this thesis, as explained in section 5.1. The results of these simulations and their significance are summarized in the next chapter.

6. RESULTS AND DISCUSSION

The primary result of the work is the parametrized force field itself, and all the parameters in it are listed in the appendix A. The purpose of the MD simulations carried out in this thesis is to test the performance of the force field and to describe the behaviour of the PBDT-TPD polymer in different polymer phases. This was done by visualizing the trajectories of different systems, determining the distance between different polymer chains in crystalline and amorphous phases and studying the distribution of the SR-CW-CH-ST dihedral angles. This chapter outlines these results and how they compare to other computational or experimental studies of D–A copolymers.

6.1 Parametrized force field

As far as we know, our modified force field for PBDT-TPD is the first one made for GROMACS [6], since the force fields in other studies by Ravva et al. [10] and Wang et al. [11] were made for LAMMPS [9], and by Jackson et al. [13] for TINKER [12]. Even though in all of these studies the OPLS-AA force field [7] was used as the basis, the form of the potential functions and the units of the parameters in LAMMPS and TINKER differ from those used by GROMACS, but they can be converted from one form to another.

For the DFT optimizations from which the force field parameters for reference bond lengths b^0_{ij} and reference angle values θ^0_{ijk} were acquired, we used the LRC functional ωB97XD [68] (with the default value for the range separation parameter ω of 0.20 bohr^{-1}) with a 6–31G** [69] basis set, and the MK [75][76] method for calculating the partial charges q. The same level of theory that was used in the studies of Ravva et al. [10] and Wang et al. [11] for bond lengths b^0_{ij} and angle values θ^0_{ijk}, but they derived partial charges from restricted electrostatic potential (RESP) [84] fitting scheme at the ωB97XD/cc-PVTZ level of theory. Jackson et al. [13] used the B3LYP hybrid functional [85][86] with a 6–31+G** [69] basis set for bond lengths b^0_{ij} and angle values θ^0_{ijk}, and acquired partial charges using the Charges from the Electrostatic Potential on a Grid (ChelpG) [87] method for electrostatic potential

fitting in Q-CHEM 4.0 [88], using B3LYP/6–31+G** [85][86][69] level of theory. All the methods seemed to produce charges of similar value, with the biggest variations ranging between 0.1–0.2 e on some aromatic carbon atoms of the backbone.

The length of the oligomer used in the DFT optimizations in this work also differs from the previous studies, since we used a trimer with side chains for the parametrization of the bonded parameters and partial charges, whereas Ravva et al. [10] and Wang et al. [11] used a monomer structure with side chains, and Jackson et al. [13] a monomer structure terminated with thiophenes with side chains. As mentioned previously in chapter 5.1, the trimer structure was chosen to take the chain end effects into account, because at the head and tail part of the polymer, the bond lengths, angles and partial charges are different from those of the middle repeating units [73]. Because our force field parameters were taken from the middle part of the trimer of the optimized structure, they mimic more accurately the structure of the repeating units of the polymer. Acquiring the bonded parameters from a trimer structure seems to especially influence the bond angles, and the differences between our reference angle values and those in the studies of Ravva et al. [10] and Jackson et al. [13] can be as large as 5°. The reference bond lengths are not affected as strongly and produce very similar results, with the biggest differences between the values being in the range of 0.002–0.003 nm.

The final difference between our force field and those of the previous studies is the parametrization of the SR-CW-CH-ST dihedral RB coefficients. Our parametrization method was explained previously in chapter 5.1, and a ωB97XD/6–31G** [68][69] level of theory was used. Jackson et al. [13] conducted the parametrization for a monomer structure with methyls as side chains, and mention that the dihedral angles for the restrained structures were performed at 10° intervals, whereas we used 5° intervals. Geometry optimizations with DFT were performed with B3LYP/6–31+G** [85][86][69], and resulting geometries were used as the input for RI-MP2/cc-pVTZ single-point energy calculations. The studies of Ravva et al. [10] and Wang et al. [11] also parametrized the dihedral using a monomer structure with methyls as side chains, and parametrized it against the results of DFT calculations carried out at the ωB97XD/6–31G** [68][69] level of theory.

In these studies the parameters for the dihedral angle were taken from the first scan. As visible from figure 5.8, performing more than one scan in our parametrization process improved the EM potential energy profile and made it converge closer to the DFT energy profile. The single biggest energy difference between the profiles in our results was 3.0 kJ mol^{-1} at $\psi = 5°$ in the fifth scan in the figure 5.8(e). In the

study of Jackson et al. [13], the differences between the two energy profiles were all lower than 2.0 kJ mol^{-1} (mentioned on page 31 of the supporting information I), and in the study of Wang et al. [11], based on figure S1(c) of the supporting information, the biggest energy difference would seem to be in the range of 4.0 kJ mol^{-1}. In all three cases the potential barrier heights and the shape of the potential curve are similar. Another difference between this work and previous studies is that for the scans we used a trimer structure with methyls as the side chains, while other studies used a monomer structure with methyls as side chains. However, in the supporting information figure S1 of the study Wang et al. [11], justification is given that a monomer is long enough for fitting of the dihedral parameters. We found this not to be the case in our studies, as the constrained geometry optimizations of the monomer structure gave a different result for the structure with the lowest energy value compared to the optimizations with the trimer structure.

It should also be noted that while our RB coefficients were parametrized for SR-CW-CH-ST dihedral angle, in the work of Ravva et al. [10] and Wang et al. [11], a dihedral angle SR-CW-CH-CM was used, and in Jackson et al. [13] a dihedral angle CS-CW-CH-ST was used. All of these describe the same dihedral torsion between BDT and TPD, and choosing through which four atoms to define the dihedral is mostly just a matter of opinion. Unfortunately this means that the parameters defined for the SR-CW-CH-ST dihedral angle in thesis cannot be compared to those in the other studies, because the dihedral angle has been defined for different atom types than in our case. However, the dihedral angle value that produces the lowest energy is close to the same value in all studies, which when defined through atoms SR-CW-CH-ST is around $\psi = -15°$, and the shape of the potential energy curves are similar in all cases. This can be noted when comparing figure 5.8 to figure S1(b) in the supporting information of [11] and to figure D15-1 in table S1 of [13], while taking into account the fact that the dihedral is defined through four different atoms in all three cases.

6.2 Molecular dynamics simulations

It was observed during the simulations that after the NVT ensemble (or the NPT ensemble in case of the solvent system) the systems had already reached a local energy minimum, which meant that the morphologies no longer changed drastically during the simulations. This means that simulation times longer than the 5 ns used here in the final production MD simulation were not necessary, as the morphologies would just continue to remain in their local energy minimum during the course of a

longer simulation. The details of the computational studies to which the results of the different simulations carried out in this thesis are compared to were presented earlier in chapter 2.4. All the figures of the polymers in this chapter have been made with the VMD software [80] using the tachyon render [81].

6.2.1 Solvent system

In the simulation of a single *anti*-conformation PBDT-TPD octamer in chloroform, the density of the system after the NPT simulation matched the experimental density of chloroform ($\approx$1.49 g cm^{-3}), which was acquired from reference [83]. The polymer in this simulation stayed relatively planar, with most of the dihedral angles between BDT and TPD changed from the *anti*-conformation starting configuration to the *syn*-conformation, as visible from figure 6.1. The type of folding observed in the vacuum simulations and discussed later in case of the amorphous system in section 6.2.3, does not occur in solvent because of the chloroform molecules restricting the chain from folding. This was also noted in reference [39], where it is stated that chain aggregation for liquid systems is only reported for polymers with a very high molecular weight.

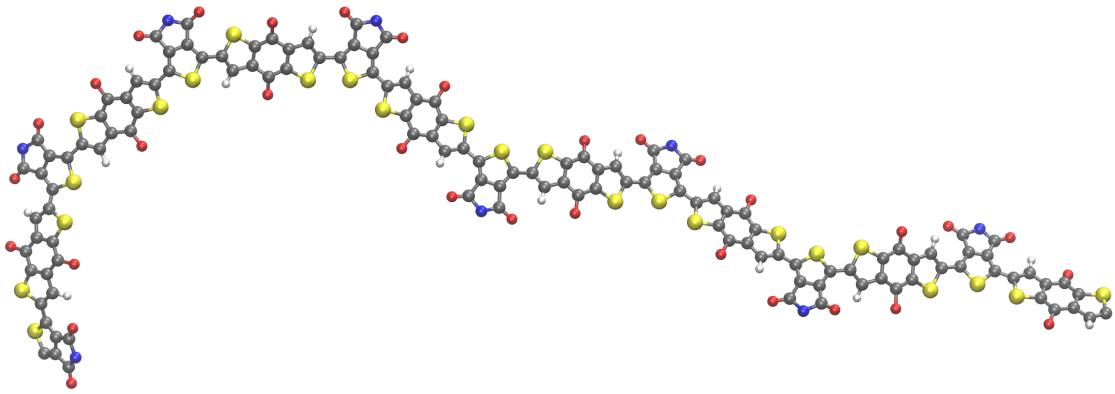

Figure 6.1 *Snapshot of the solvent system of a single PBDT-TPD octamer in chloroform. Side chains and the chloroform solvent molecules are not shown for clarity.*

6.2.2 Crystalline phase

Figures 6.2 and 6.3 illustrate the morphologies of the crystalline systems during the simulations. The simulation of the *syn*-conformation produced a surprising result. Despite the starting structure of system being two stacks of three polymers on top

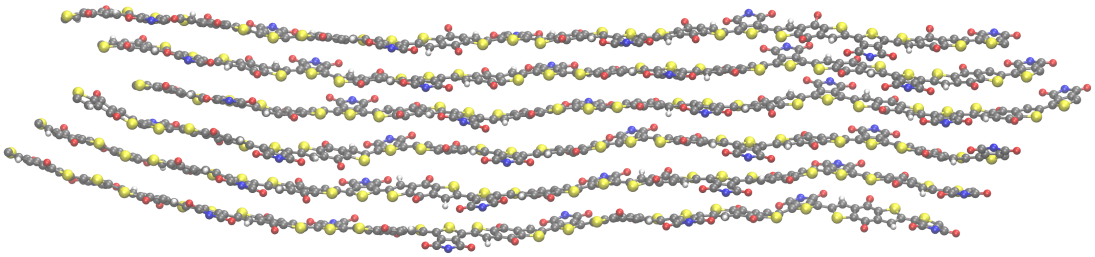

Figure 6.2 *Snapshot of the crystalline structure of six PBDT-TPD octamers with the syn-conformation as the starting structure. Side chains are not shown for clarity.*

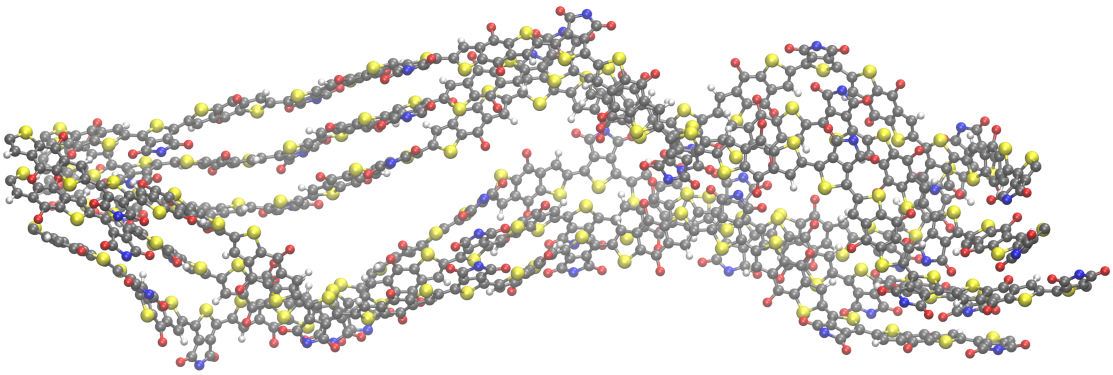

Figure 6.3 *Snapshot of the crystalline structure of six PBDT-TPD octamers with the anti-conformation as the starting structure. Side chains are not shown for clarity.*

of each other as illustrated in figure 5.9, the simulations produced a trajectory where the other stack as a whole moved on top of the neighbouring stack, resulting in a morphology where all six polymer chains are on top of each other in a single stack, as illustrated in figure 6.2. The same type of behaviour is also observed in the simulation of the crystalline phase with the *anti*-conformation chains as the starting conformers. The different chains in the same stack keep closely together, but the different stacks start to twist around each other, resulting in a semicrystalline morphology visible from figure 6.3.

It is possible that this conformation was also at first moving towards the single stack morphology, but as mentioned previously, the system had reached a local minimum, and no significant changes in the system were observed from the trajectory. The differences in resulting morphologies here are also influenced by the dihedral angle torsion between BDT and TPD moieties, because as discussed later in this chapter, the *syn*-conformation is a more favourable conformation for the polymer than the *anti*-conformation. This means that more dihedral angle torsion affecting the morphology will be happening in the simulation of the *anti*-conformation system.

Additionally, the polymers chains with the *anti*- and *syn*-conformations were in the beginning stacked in identical layers, meaning that under one BDT (or TPD) moiety was another BDT (or TPD) moeity of a different chain, respectively. This seems to change a bit during the simulations, as the chains shift more towards configurations where BDT and TPD moieties of different chains are closer to each other, which corresponds to the desired active layer morphology of PSCs [4]. However, the large side chains and the interactions between the backbones of the different chains in the crystalline morphologies restrict the movement of the chains in these systems not allowing the them to slide freely between each other.

6.2.3 Amorphous phase

Unlike in the crystalline structures, in the beginning of the simulation of the amorphous morphology different polymer chains had more freedom to move around each other, as visible from figure 5.10. The structure resulting from the simulation of the amorphous system is illustrated in figure 6.4. The different chains fold around each other, resulting in a much more random self-aggregated configuration than observed in the crystalline morphologies. The folding of the chains produces quite sharp curvature in some bends, and the same type of behaviour has been observed

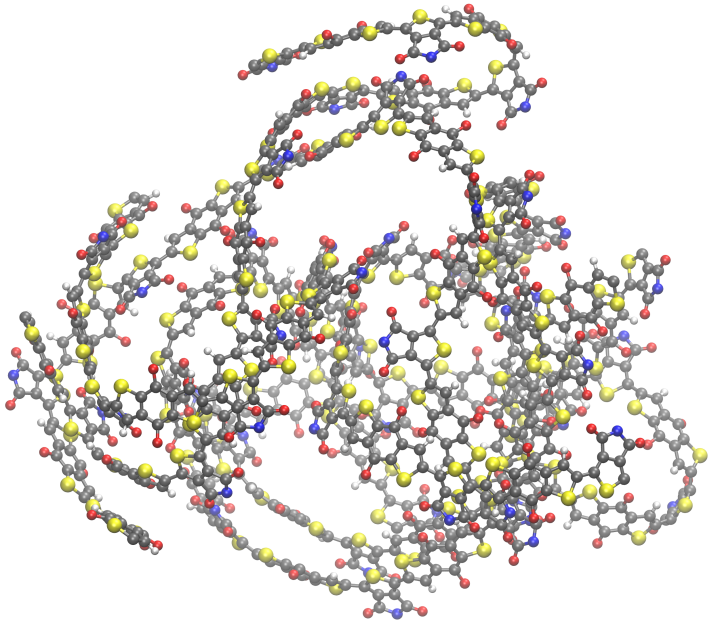

Figure 6.4 *Snapshot of the amorphous structure of six PBDT-TPD octamers. Side chains are not shown for clarity.*

in the other studies of D–A copolymers in vacuum systems. For example, in the study of Caddeo et al. [39], high flexibility and chain folding was observed for a P(NDI2OD-T2) polymer, and in the study of Jackson et al. [13], the single PBDT-TPD with 30 CRUs was determined to have a conformational class of a stacked rod.

6.2.4 π-stacking distances

The average distance between two polymer chains in the same stack, expressed with a technical term π-stacking distance, was also determined from the trajectories. This was done by choosing from the trajectory D and A residues in the polymer backbones in different chains that stayed in close contact to each other during the whole simulation, and calculating the distance between the centers of mass of these residues. For each system, four suitable pairs from different chains were chosen and the distances were calculated from the production run trajectory every 0.1 ps, after which the total average of all the distance values was taken.

These gave a π-stacking distance of **3.8 Å** for the crystalline morphologies and 3.9 Å for the amorphous morphology. The lamellar stacking distance, which is the distance between two chains next to each other in the two stacks, could not be determined, because as mentioned previously, the two stacks in the crystalline morphologies tended to twist around and on top of each other in the simulations. The experimental π-stacking distance for D–A copolymers containing either a BDT or a TPD moiety has been reported to be in the range of 3.8–4.2 Å [89][90][91], and specifically for PBDT-TPD, Piliego et al. [92] reported a π-stacking distance of **3.6 Å**. These are in the same range as the values determined for the D–A π-stacking distance in this thesis, which means that the modified force field used in the simulations produces results that match experimental studies.

The small difference of 0.2 Å between our computational π-stacking value of 3.8 Å and the experimental value of 3.6 Å in the study of Piligo et al. [92] can be accounted to the fact that the manufacturing process of the PSC was not taken into account in the simulations. At least in the simulation of amorphous systems in reference [38], this self-aggregated method was noted to produce morphologies further from the equilibrium than melt-quenched systems, which were first simulated in a higher temperature and then cooled to room temperature. Our simulations also only used stacks containing three polymers on top of each other, meaning that there is more room for the top and bottoms chains to move further away from the middle chain than there would be in an infinite crystal. This would cause the π-stacking distance

to have a larger value than in the experimental results. The method of calculating the distance from the trajectories by using the centers of mass of neighbouring residues also plays a role, as other methods might produce varying results.

6.2.5 Dihedral distributions

Final thing determined to examine the conformation of the chains in different systems was the distribution of the SR-CW-CH-ST dihedral. These are presented for all three different morphologies in figure 6.5, where the ψ values near zero correspond to the *syn*-conformation, and values near -180° or 180° to the *anti*-conformation.

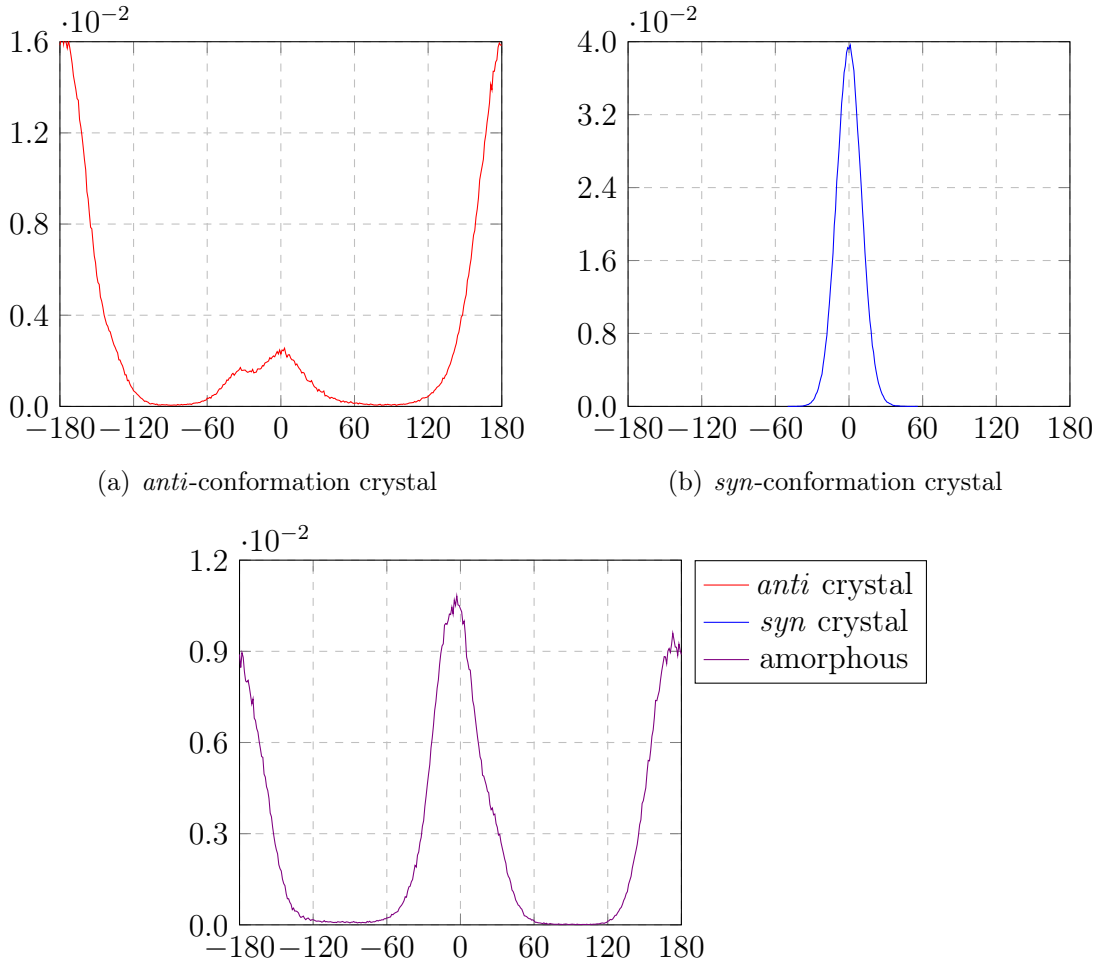

(a) *anti*-conformation crystal

(b) *syn*-conformation crystal

(c) Amorphous

Figure 6.5 *Dihedral distributions of the SR-CW-CH-ST dihedral in the simulations of the syn-conformation crystal (a), anti-conformation crystal (b) and the amorphous phase (c). All x-axes have the units of degree for the dihedral angle ψ and percent probability for the y-axes.*

As expected, in the crystalline morphologies the dihedral angle is mostly in the same conformation as in the starting structure, because of the other nearby polymer chains and large side chains, the dihedral does not have much space to twist to the other conformation. A small fraction of the dihedrals in the *anti*-conformation crystalline phase have twisted to *syn*-conformation, as visible from figure 6.5(a), but none of the dihedrals in the *syn*-conformation crystalline phase have changed to *anti*-conformation, as visible from figure 6.5(b). The dihedral distribution in the amorphous morphology in figure 6.5(c) shows that this system contains both conformations of the dihedral in almost equal amounts. This is a similar result to the dihedral distribution obtained by Jackson et al. [13] in the simulation of a single polymer with 30 CRUs in vacuum, as visible from the plot on the page S27 in the supporting information.

These results confirm that the *syn*-conformation is more desirable for the polymer than the *anti*-conformation, which was also the case according to DFT calculations when parametrizing the RB coefficients for the dihedral, and the same result was obtained also by other computational studies [10][11][13]. This is because in the *syn*-conformation a hydrogen from BDT and oxygen from TPD (atom types HA and O in figure 5.5) are able to form a hydrogen bond. However, this does not mean that the polymer would only exist in this conformation, as observed from the simulation of the amorphous simulation, which contained both conformations in nearly equal amounts.

7. CONCLUSIONS

To achieve higher PCEs in organic solar cells, optimizing the morphology of the active layer is crucial. To allow as many excitons as possible to dissociate into electrons and holes, the surface area between the donor and acceptor phases must be maximized and the distance between the phases must be smaller than the diffusion length. Both phases must also form a continuous network so that after charge separation the charges can be transferred to the electrodes. The optimization of the morphology of the active layer and understanding how different factors affect it is an active challenge in the field. One possible method for studying it is by computational methods which help in visualizing and in suggesting possible behaviour of these systems. In the case of MD simulations, a force field that accurately describes the studied polymer and how different atoms in it interact with each other is required.

The goal of thesis was to outline the methods for the parametrization of such a force field for PBDT-TPD polymer to be used with GROMACS software [6], and test how it performs in MD simulations by comparing theresults to previous experimental and computational studies. This was done by using the OPLS-AA force field [7] as a template, and optimizing a PBDT-TPD trimer structure in DFT calculations with a ωB97XD/6–31G** [68][69] level of theory to obtain bond, angle and partial charge parameters for the new modified force field. The RB parameters for the dihedral angle between the BDT and TPD moieties were also newly parametrized, because this dihedral determines the conformation of the polymer backbone, and therefore accurate parameters for it are important [5][13][39]. The simulations of the polymer in solvent in both crystalline and amorphous phases with the new parametrized force field confirmed that it produced results that were comparable to previous studies, and therefore accurately described the behaviour of the PBDT-TPD polymer.

With the force field parametrized in this thesis, further computational studies containing the PBDT-TPD polymer can be carried out. For example one interesting research topic would be morphological studies which take into account the manufacturing process of the PSC by simulating the systems first in an elevated temperature, and then cooling them to room temperature. The methods outlining the force field

parametrization process can also be used for other polymers, such as polymers used as the eA molecule in the active layer. After this simulations of different systems that contain both the eD and eA can be carried out to obtain information about the morphology of the active layer mixed eD–eA blend, and not just parts of it.

BIBLIOGRAPHY

[1] **Wang, Q., Xie, Y., Soltani-Kordshuli, F., and Eslamian, M.**, Progress in Emerging Solution-Processed Thin Film Solar Cells – Part I: Polymer Solar Cells. *Renewable and Sustainable Energy Reviews*, 56(1): 347–361. 2016.

[2] **Scharber, M.C. and Sariciftci, N.S.**, Efficiency of Bulk-Heterojunction Organic Solar Cells. *Progress in Polymer Science*, 38(12): 1929–1940. 2013.

[3] **Hoppe, H. and Sariciftci, N.S.**, Organic Solar Cells: An Overview. *Journal of Materials Research*, 19(7): 1924–1945. 2004.

[4] **Dou, L., Liu, Y., Hong, Z., Li, G., and Yang, Y.**, Low-Bandgap Near-IR Conjugated Polymers/Molecules for Organic Electronics. *Chemical Reviews*, 115(23): 12633–12665. 2015.

[5] **Do, K., Ravva, M.K., Wang, T., and Brédas, J.L.**, Computational Methodologies for Developing Structure–Morphology–Performance Relationships in Organic Solar Cells: A Protocol Review. *Chemistry of Materials*, 29(1): 346–354. 2016.

[6] **Abraham, M.J., van de Spoel, D., Lindahl, E., Hess, B., and the GROMACS development team**, *GROMACS User Manual version 5.1.2*. `www.gromacs.org`, 2016.

[7] **Jorgensen, W.L. and Tirado-Rives, J.**, Potential Energy Functions for Atomic-Level Simulations of Water and Organic and Biomolecular Systems. *Proceedings of the National Academy of Sciences of the United States of America*, 102(19): 6665–6670. 2005.

[8] **Frisch, M.J., Trucks, G.W., Schlegel, H.B., Scuseria, G.E., Robb, M.A., Cheeseman, J.R., Scalmani, G., Barone, V., Petersson, G.A., Nakatsuji, H., et al.**, Gaussian 16, Revision D.01. Gaussian Inc., Wallingford, Connecticut, 2016.

[9] **Plimpton, S.**, Fast Parallel Algorithms for Short-Range Molecular Dynamics. *Journal of Computational Physics*, 117(1): 1–19. 1995.

[10] **Ravva, M.K., Wang, T., and Brédas, J.L.**, Nature of the Binding Interactions between Conjugated Polymer Chains and Fullerenes in Bulk Heterojunction Organic Solar Cells. *Chemistry of Materials*, 28(22): 8181–8189. 2016.

[11] **Wang, T., Ravva, M.K., and Brédas, J.L.**, Impact of the Nature of the Side-Chains on the Polymer-Fullerene Packing in the Mixed Regions of Bulk Heterojunction Solar Cells. *Advanced Functional Materials*, 26(32): 5913–5921. 2016.

[12] **Ponder, J.W. et al.**, TINKER: Software Tools for Molecular Design. *Washington University School of Medicine, Saint Louis, Missouri*. 2004.

[13] **Jackson, N.E., Kohlstedt, K.L., Savoie, B.M., Olvera de la Cruz, M., Schatz, G.C., Chen, L.X., and Ratner, M.A.**, Conformational Order in Aggregates of Conjugated Polymers. *Journal of the American Chemical Society*, 137(19): 6254–6262. 2015.

[14] **Choubey, P., Oudhia, A., and Dewangan, R.**, A Review: Solar Cell Current Scenario and Future Trends. *Recent Research in Science and Technology*, 4(8): 99–101. 2012.

[15] **Vivo, P.** Multilayered Thin Films for Organic Photovoltaics, dissertation, *Tampere University of Technology*, Publication 918, 2010.

[16] **Guo, X., Zhou, N., Lou, S.J., Smith, J., Tice, D.B., Hennek, J.W., Ortiz, R.P., Navarrete, J.T.L., Li, S., Strzalka, J., et al.**, Polymer Solar Cells with Enhanced Fill Factors. *Nature Photonics*, 7(10): 825–833. 2013.

[17] **Becquerel, E.**, On Electron Effects Under the Influence of Solar Radiation. *Comptes Rendues*, 9: 561. 1839.

[18] **Engel, T. and Reid, P.**, *Physical Chemistry*. Pearson Prentice Hall, 2nd edition, Upper Saddle River, New Jersey, USA. 2010.

[19] **Zumdahl, S.S.**, *Chemical Principles*. Brooks/Cole, 6th edition, Belmont, California, USA. 2009.

[20] KhanAcademy, Picture of the electromagnetic spectrum, available `https://www.khanacademy.org/science/physics/light-waves/`, accessed 20.5.2017.

[21] **Tipler, P.A. and Llewellyn, R.A.**, *Modern Physics*. W.H. Freeman and Company, 5th edition, New York, New York, USA. 2008.

[22] **Dennler, G., Scharber, M.C., and Brabec, C.J.**, Polymer-Fullerene Bulk-Heterojunction Solar Cells. *Advanced Materials*, 21(13): 1323–1338. 2009.

[23] Wikimedia Commons, Picture of the HOMO–LUMO transition, available `https://en.wikipedia.org/wiki/File:Molecule_HOMO-LUMO_diagram.svg`, accessed 20.5.2017.

[24] **Green, M.A., Emery, K., Hishikawa, Y., Warta, W., Dunlop, E.D., Levi, D.H., and Ho-Baillie, A.W.Y.**, Solar Cell Efficiency Tables (version 49). *Progress in Photovoltaics: Research and Applications*, 25(1): 3–13. 2017.

[25] **Liang, Y., Xu, Z., Xia, J., Tsai, S.T., Wu, Y., Li, G., Ray, C., and Yu, L.**, For the Bright Future – Bulk Heterojunction Polymer Solar Cells with Power Conversion Efficiency of 7.4%. *Advanced Materials*, 22(20): 135–138. 2010.

[26] **Kumaresan, P., Vegiraju, S., Ezhumalai, Y., Yau, S.L., Kim, C., Lee, W.H., and Chen, M.C.**, Fused-Thiophene Based Materials for Organic Photovoltaics and Dye-Sensitized Solar Cells. *Polymers*, 6(10): 2645–2669. 2014.

[27] **Hains, A.W., Liang, Z., Woodhouse, M.A., and Gregg, B.A.**, Molecular Semiconductors in Organic Photovoltaic Cells. *Chemical reviews*, 110(11): 6689–6735. 2010.

[28] **Ameri, T., Li, N., and Brabec, C.J.**, Highly Efficient Organic Tandem Solar Cells: A Follow Up Review. *Energy & Environmental Science*, 6(8): 2390–2413. 2013.

[29] **Dennler, G., Scharber, M.C., Ameri, T., Denk, P., Forberich, K., Waldauf, C., and Brabec, C.J.**, Design Rules for Donors in Bulk-Heterojunction Tandem Solar Cells Towards 15% Energy-Conversion Efficiency. *Advanced Materials*, 20(3): 579–583. 2008.

[30] **Alam, M. and Cameron, D.**, Optical and Electrical Properties of Transparent Conductive ITO Thin Films Deposited by Sol–Gel Process. *Thin Solid Films*, 377: 455–459. 2000.

[31] **Zhou, Y., Fuentes-Hernandez, C., Shim, J., Meyer, J., Giordano, A.J., Li, H., Winget, P., Papadopoulos, T., Cheun, H., Kim, J., et al.**, A Universal Method to Produce Low-Work Function Electrodes for Organic Electronics. *Science*, 336(6079): 327–332. 2012.

[32] **Havinga, E.E., ten Hoeve, W., and Wynberg, H.**, A New Class of Small Band Gap Organic Polymer Conductors. *Polymer Bulletin*, 29(1): 119–126. 1992.

[33] **Nakabayashi, K. and Mori, H.**, Donor-Acceptor Block Copolymers: Synthesis and Solar Cell Applications. *Materials*, 7(4): 3274–3290. 2014.

[34] **Zhou, H., Yang, L., and You, W.**, Rational Design of High Performance Conjugated Polymers for Organic Solar Cells. *Macromolecules*, 45(2): 607–632. 2012.

[35] **Koeppe, R. and Sariciftci, N.**, Photoinduced Charge and Energy Transfer Involving Fullerene Derivatives. *Photochemical & Photobiological Sciences*, 5(12): 1122–1131. 2006.

[36] **Clarke, T.M. and Durrant, J.R.**, Charge Photogeneration in Organic Solar Cells. *Chemical Reviews*, 110(11): 6736–6767. 2010.

[37] **Barford, W. and Marcus, M.**, Perspective: Optical Spectroscopy in π-Conjugated Polymers and How It Can Be Used to Determine Multiscale Polymer Structures. *The Journal of Chemical Physics*, 146(13): 130902. 2017.

[38] **Root, S.E., Jackson, N.E., Savagatrup, S., Arya, G., and Lipomi, D.J.**, Modelling the Morphology and Thermomechanical Behaviour of Low-Bandgap Conjugated Polymers and Bulk Heterojunction Films. *Energy & Environmental Science*, 10(2): 558–569. 2017.

[39] **Caddeo, C., Fazzi, D., Caironi, M., and Mattoni, A.**, Atomistic Simulations of P (NDI2OD-T2) Morphologies: From Single Chain to Condensed Phases. *The Journal of Physical Chemistry B*, 118(43): 12556–12565. 2014.

[40] **Case, D.A., Cheatham, T.E., Darden, T., Gohlke, H., Luo, R., Merz, K.M., Onufriev, A., Simmerling, C., Wang, B., and Woods, R.J.**, The AMBER Biomolecular Simulation Programs. *Journal of Computational Chemistry*, 26(16): 1668–1688. 2005.

[41] **Duan, Y., Wu, C., Chowdhury, S., Lee, M.C., Xiong, G., Zhang, W., Yang, R., Cieplak, P., Luo, R., Lee, T., et al.**, A Point-Charge Force Field for Molecular Mechanics Simulations of Proteins Based on Condensed-Phase Quantum Mechanical Calculations. *Journal of Computational Chemistry*, 24(16): 1999–2012. 2003.

[42] **Wang, J., Wolf, R.M., Caldwell, J.W., Kollman, P.A., and Case, D.A.**, Development and Testing of a General Amber Force Field. *Journal of Computational Chemistry*, 25(9): 1157–1174. 2004.

[43] **Phillips, J.C., Braun, R., Wang, W., Gumbart, J., Tajkhorshid, E., Villa, E., Chipot, C., Skeel, R.D., Kale, L., and Schulten, K.**, Scalable Molecular Dynamics with NAMD. *Journal of Computational Chemistry*, 26(16): 1781–1802. 2005.

[44] **Do, K., Saleem, Q., Ravva, M.K., Cruciani, F., Kan, Z., Wolf, J., Hansen, M.R., Beaujuge, P.M., and Brédas, J.L.**, Impact of Fluorine Substituents on π-Conjugated Polymer Main-Chain Conformations, Packing, and Electronic Couplings. *Advanced Materials*, 28(37): 8197–8205. 2016.

[45] **Berendsen, H.J.**, *Simulating the Physical World: Hierarchical Modeling from Quantum Mechanics to Fluid Dynamics*. Cambridge University Press, 1st edition, Cambridge, England, UK. 2007.

[46] **Jensen, F.**, *Introduction to Computational Chemistry*. John Wiley & Sons, 2nd edition, Chichester, England, UK. 2007.

[47] **Brooks, B.R., Brooks, C.L., MacKerell, A.D., Nilsson, L., Petrella, R.J., Roux, B., Won, Y., Archontis, G., Bartels, C., Boresch, S., et al.**, CHARMM: The Biomolecular Simulation Program. *Journal of Computational Chemistry*, 30(10): 1545–1614. 2009.

[48] **Scott, W.R., Hünenberger, P.H., Tironi, I.G., Mark, A.E., Billeter, S.R., Fennen, J., Torda, A.E., Huber, T., Krüger, P., and van Gunsteren, W.F.**, The GROMOS Biomolecular Simulation Program Package. *The Journal of Physical Chemistry A*, 103(19): 3596–3607. 1999.

[49] **Morse, P.M.**, Diatomic Molecules According to the Wave Mechanics. II. Vibrational Levels. *Physical Review*, 34(1): 57–64. 1929.

[50] **Schlick, T.**, *Molecular Modeling and Simulation: An Interdisciplinary Guide*. Springer Science & Business Media, 2nd edition, New York, New York, USA. 2010.

[51] **Cramer, C.J.**, *Essentials of Computational Chemistry: Theories and Models*. John Wiley & Sons, 2nd edition, Chichester, England, UK. 2004.

[52] **Verlet, L.**, Computer "Experiments" on Classical Fluids. I. Thermodynamical Properties of Lennard-Jones Molecules. *Physical Review*, 159(1): 98–103. 1967.

[53] **Salvato-Vallverdu, G.** Picture of periodic boundary conditions, available `http://www.texample.net/tikz/examples/periodic-boundaries-conditions/`, accessed 23.2.2017.

[54] **Berendsen, H.J., Postma, J.v., van Gunsteren, W.F., DiNola, A., and Haak, J.**, Molecular Dynamics with Coupling to An External Bath. *The Journal of Chemical Physics*, 81(8): 3684–3690. 1984.

[55] **Bussi, G., Donadio, D., and Parrinello, M.**, Canonical Sampling Through Velocity Rescaling. *The Journal of Chemical Physics*, 126(1): 014101. 2007.

[56] **Evans, D.J. and Holian, B.L.**, The Nose–Hoover Thermostat. *The Journal of Chemical Physics*, 83(8): 4069–4074. 1985.

[57] **Martoňák, R., Laio, A., and Parrinello, M.**, Predicting Crystal Structures: The Parrinello–Rahman Method Revisited. *Physical Review Letters*, 90(7): 075503. 2003.

[58] **Martyna, G.J., Tuckerman, M.E., Tobias, D.J., and Klein, M.L.**, Explicit Reversible Integrators for Extended Systems Dynamics. *Molecular Physics*, 87(5): 1117–1157. 1996.

[59] **Atkins, P.W. and Friedman, R.S.**, *Molecular Quantum Mechanics*. Oxford University Press, 5th edition, New York, New York, USA. 2011.

[60] **Aittala, P.** Computational Study of Charge Transfer in a Porphine–Quinone Complex and Novel Alkoxypyridylindolizine Derivatives, dissertation, *Tampere University of Technology*, Publication 936, 2010.

[61] **Thomas, L.H.**, The Calculation of Atomic Fields. *Mathematical Proceedings of the Cambridge Philosophical Society*, 23(5): 542–548. 1927.

[62] **Fermi, E.**, Statistical Method to Determine Some Properties of Atoms. *Rendiconti Accademia Nazionale Lincei*, 6(1): 602–607. 1927.

[63] **Toivonen, T.** Computational Study of Photoinduced Energy Transfer of Porphyrin-Fullerene and Oligo(p-phenylenevinylene)-Fullerene Dyads, dissertation, *Tampere University of Technology*, Publication 700, 2007.

[64] **Hohenberg, P. and Kohn, W.**, Inhomogeneous Electron Gas. *Physical Review*, 136(3B): B864. 1964.

[65] **Kohn, W. and Sham, L.J.**, Self-Consistent Equations Including Exchange and Correlation Effects. *Physical Review*, 140(4A): A1133. 1965.

[66] **Cramariuc, O.** Computational Characterization of Photoabsorption and Structure of Porphyrin-Fullere Dyads, dissertation, *Tampere University of Technology*, Publication 644, 2006.

[67] **Slater, J.C.**, A Simplification of the Hartree–Fock Method. *Physical Review*, 81(3): 385–390. 1951.

[68] **Chai, J.D. and Head-Gordon, M.**, Long-Range Corrected Hybrid Density Functionals with Damped Atom–Atom Dispersion Corrections. *Physical Chemistry Chemical Physics*, 10(44): 6615–6620. 2008.

[69] **Hehre, W.J., Stewart, R.F., and Pople, J.A.**, Self-Consistent Molecular-Orbital Methods. I. Use of Gaussian Expansions of Slater-Type Atomic Orbitals. *The Journal of Chemical Physics*, 51(6): 2657–2664. 1969.

[70] Avogadro: An Open-Source Molecular Builder and Visualization Tool. Version 1.2.0. `https://avogadro.cc/`, accessed 25.4.2017.

[71] **Hanwell, M.D., Curtis, D.E., Lonie, D.C., Vandermeersch, T., Zurek, E., and Hutchison, G.R.**, Avogadro: An Advanced Semantic Chemical Editor, Visualization, and Analysis platform. *Journal of Cheminformatics*, 4(1): 17. 2012.

[72] **Cabanetos, C., El Labban, A., Bartelt, J.A., Douglas, J.D., Mateker, W.R., Frechet, J.M., McGehee, M.D., and Beaujuge, P.M.**, Linear Side Chains in Benzo[1,2-*b*:4,5-*b*']dithiophene–Thieno[3,4-*c*]pyrrole-4,6-dione Polymers Direct Self-Assembly and Solar Cell Performance. *Journal of the American Chemical Society*, 135(12): 4656–4659. 2013.

[73] **Jacquemin, D. and Adamo, C.**, Bond Length Alternation of Conjugated Oligomers: Wave Function and DFT Benchmarks. *Journal of Chemical Theory and Computation*, 7(2): 369–376. 2010.

[74] **Poelking, C. and Andrienko, D.**, Effect of Polymorphism, Regioregularity and Paracrystallinity on Charge Transport in Poly(3-hexylthiophene) [P3HT] Nanofibers. *Macromolecules*, 46(22): 8941–8956. 2013.

[75] **Besler, B.H., Merz, K.M., and Kollman, P.A.**, Atomic Charges Derived from Semiempirical Methods. *Journal of Computational Chemistry*, 11(4): 431–439. 1990.

[76] **Singh, U.C. and Kollman, P.A.**, An Approach to Computing Electrostatic Charges for Molecules. *Journal of Computational Chemistry*, 5(2): 129–145. 1984.

[77] OPLS Force Field Parameters for Chloroform, files "trichloromethane.itp" and "trichloromethane_T298.15.pdb.qz", Virtual Chemistry website,

available `http://virtualchemistry.org/molecule.php?filename=trichloromethane.zmat`, accessed 29.6.2017.

[78] **Caleman, C., van Maaren, P.J., Hong, M., Hub, J.S., Costa, L.T., and van der Spoel, D.**, Force Field Benchmark of Organic Liquids: Density, Enthalpy of Vaporization, Heat Capacities, Surface Tension, Isothermal Compressibility, Volumetric Expansion Coefficient, and Dielectric Constant. *Journal of Chemical Theory and Computation*, 8(1): 61–74. 2012.

[79] **van der Spoel, D., van Maaren, P.J., and Caleman, C.**, GROMACS Molecule & Liquid Database. *Bioinformatics*, 28(5): 752–753. 2012.

[80] **Humphrey, W., Dalke, A., and Schulten, K.**, VMD – Visual Molecular Dynamics. *Journal of Molecular Graphics*, 14(1): 33–38. 1996.

[81] **Stone, J.**, An Efficient Library for Parallel Ray Tracing and Animation. Master's thesis, Computer Science Department, University of Missouri-Rolla. 1998.

[82] **Hockney, R.W. and Eastwood, J.W.**, *Computer Simulation Using Particles*. Taylor & Francis Group, 1st edition, New York, New York, USA. 1988.

[83] **Haynes, W.M.**, *CRC Handbook of Chemistry and Physics*. CRC Press, 97th edition, Boca Raton, Florida, USA. Table "Compressibility and Expansion Coefficients of Liquids" and table "Physical Constants of Organic Compounds" `www.hbcponline.com/`. 2016.

[84] **Bayly, C.I., Cieplak, P., Cornell, W., and Kollman, P.A.**, A Well-Behaved Electrostatic Potential Based Method Using Charge Restraints for Deriving Atomic Charges: The RESP Model. *The Journal of Physical Chemistry*, 97(40): 10269–10280. 1993.

[85] **Becke, A.D.**, A New Mixing of Hartree–Fock and Local Density-Functional Theories. *The Journal of Chemical Physics*, 98(2): 1372–1377. 1993.

[86] **Lee, C., Yang, W., and Parr, R.G.**, Development of the Colle–Salvetti Correlation-Energy Formula Into a Functional of the Electron Density. *Physical Review B*, 37(2): 785–789. 1988.

[87] **Breneman, C.M. and Wiberg, K.B.**, Determining Atom-Centered Monopoles from Molecular Electrostatic Potentials. The Need for High Sampling Density in Formamide Conformational Analysis. *Journal of Computational Chemistry*, 11(3): 361–373. 1990.

[88] **Shao, Y., Molnar, L.F., Jung, Y., Kussmann, J., Ochsenfeld, C., Brown, S.T., Gilbert, A.T., Slipchenko, L.V., Levchenko, S.V., O'Neill, D.P., et al.**, Advances in Methods and Algorithms in a Modern Quantum Chemistry Program Package. *Physical Chemistry Chemical Physics*, 8(27): 3172–3191. 2006.

[89] **Son, H.J., Wang, W., Xu, T., Liang, Y., Wu, Y., Li, G., and Yu, L.**, Synthesis of Fluorinated Polythienothiophene-*co*-benzodithiophenes and Effect of Fluorination on the Photovoltaic Properties. *Journal of the American Chemical Society*, 133(6): 1885–1894. 2011.

[90] **Hammond, M.R., Kline, R.J., Herzing, A.A., Richter, L.J., Germack, D.S., Ro, H.W., Soles, C.L., Fischer, D.A., Xu, T., Yu, L., et al.**, Molecular Order in High-Efficiency Polymer/Fullerene Bulk Heterojunction Solar Cells. *ACS Nano*, 5(10): 8248–8257. 2011.

[91] **Chu, T.Y., Lu, J., Beaupré, S., Zhang, Y., Pouliot, J.R., Zhou, J., Najari, A., Leclerc, M., and Tao, Y.**, Effects of the Molecular Weight and the Side-Chain Length on the Photovoltaic Performance of Dithienosilole/Thienopyrrolodione Copolymers. *Advanced Functional Materials*, 22(11): 2345–2351. 2012.

[92] **Piliego, C., Holcombe, T.W., Douglas, J.D., Woo, C.H., Beaujuge, P.M., and Fréchet, J.M.**, Synthetic Control of Structural Order in *N*-Alkylthieno[3,4-*c*]pyrrole-4,6-dione-Based Polymers for Efficient Solar Cells. *Journal of the American Chemical Society*, 132(22): 7595–7597. 2010.

APPENDIX A. FORCE FIELD PARAMETERS

Table A1 *Parameters for the bonds between different atom types in PBDT-TPD.*

Bond		b_{ij}^0 (nm)	k_{ij}^b (kJ mol^{-1})
SR	CW	0.17615	209340.0
CW	CS	0.13632	457198.6
CS	CA1	0.14287	392721.8
CA1	CA2	0.14165	374299.9
CA2	SR	0.17458	209340.0
CS	HA	0.10829	307311.1
CA1	CR	0.14001	392721.8
CR	CA2	0.13876	392721.8
CR	OS	0.13633	376812.0
CH	ST	0.17513	209340.0
CM	CM	0.14212	392721.8
C	CM	0.14829	334944.0
C	N	0.13993	410306.4
C	O	0.12110	477295.2
CM	CH	0.13667	457198.6
CW	CH	0.14503	319871.5
CE	OS	0.14347	267955.2
N	CT	0.14517	282190.3
CE	CE	0.15290	224262.4
CE	HC	0.10900	284512.0
CT	CT	0.15290	224262.4
CT	HC	0.10900	284512.0

Table A2 *Parameters for the angles between different atom types in PBDT-TPD backbone.*

Angle			θ^0_{ijk} (deg)	k^θ_{ijk} (kJ mol^{-1} rad^{-2})
SR	CW	CS	112.721	586.152
CW	CS	CA1	113.366	586.152
CS	CA1	CA2	111.468	586.152
CA1	CA2	SR	112.053	586.152
CA2	SR	CW	90.392	619.232
CW	CS	HA	124.016	293.076
CA1	CS	HA	122.618	293.076
CS	CA1	CR	128.926	711.756
SR	CA2	CR	125.369	586.152
CA1	CR	CA2	117.816	527.537
CR	CA2	CA1	122.578	711.756
CA2	CA1	CR	119.606	711.756
CA1	CR	OS	121.734	586.152
CA2	CR	OS	120.450	586.152
CH	ST	CH	93.872	619.232
CM	CM	CH	114.597	586.152
ST	CH	CM	108.467	586.152
C	CM	CH	137.285	586.152
CM	C	N	105.016	586.152
C	N	C	113.732	586.152
C	CM	CM	108.118	586.152
N	C	O	124.590	669.888
CM	C	O	130.394	669.888
CS	CW	CH	124.335	586.152
SR	CW	CH	122.944	586.152
CM	CH	CW	133.247	586.152
ST	CH	CW	118.286	586.152
CE	OS	CR	114.818	628.020
OS	CE	HC	109.278	293.076
CE	CE	OS	109.500	418.400
C	N	CT	123.134	418.680
HC	CT	N	107.140	293.076
CT	CT	N	115.000	669.440

Table A3 *Parameters for the angles between different atom types in PBDT-TPD side chains.*

Angle			θ^0_{ijk} (deg)	k^θ_{ijk} (kJ mol^{-1} rad^{-2})
CE	CE	CE	112.700	488.273
CE	CE	HC	110.700	313.800
HC	CE	HC	107.800	276.144
CT	CT	CT	112.700	488.273
CT	CT	HC	110.700	313.800
HC	CT	HC	107.800	276.144

Table A4 *Parameters for the RB type proper dihedrals between different atom types in PBDT-TPD. All the coefficients have the units of kJ mol^{-1}.*

Proper dihedral				C_0	C_1	C_2	C_3	C_4	C_5
SR	CW	CH	ST	29.49537	7.77359	-31.40990	2.43505	6.46315	-0.06355
CA1	CR	OS	CE	12.55200	0.00000	-12.55200	0.00000	0.00000	0.00000
CA2	CR	OS	CE	12.55200	0.00000	-12.55200	0.00000	0.00000	0.00000
CR	OS	CE	CE	1.71544	2.84512	1.04600	-5.60656	0.00000	0.00000
CR	OS	CE	HC	1.58992	4.76976	0.00000	-6.35968	0.00000	0.00000
OS	CE	CE	CE	2.87441	0.58158	2.09200	-5.54798	0.00000	0.00000
OS	CE	CE	HC	0.97905	2.93716	0.00000	-3.91622	0.00000	0.00000
C	N	CT	CT	-4.70700	2.92043	1.78657	0.00000	0.00000	0.00000
C	N	CT	HC	-0.29079	-0.87237	0.00000	1.16315	0.00000	0.00000
N	CT	CT	CT	5.48732	0.02720	0.00000	-5.51451	0.00000	0.00000
N	CT	CT	HC	0.97069	2.91206	0.00000	-3.88275	0.00000	0.00000
CE	CE	CE	CE	2.92880	-1.46440	0.20920	-1.67360	0.00000	0.00000
CE	CE	CE	HC	0.62760	1.88280	0.00000	-2.51040	0.00000	0.00000
HC	CE	CE	HC	0.62760	1.88280	0.00000	-2.51040	0.00000	0.00000
CT	CT	CT	CT	2.92880	-1.46440	0.20920	-1.67360	0.00000	0.00000
CT	CT	CT	HC	0.62760	1.88280	0.00000	-2.51040	0.00000	0.00000
HC	CT	CT	HC	0.62760	1.88280	0.00000	-2.51040	0.00000	0.00000

Table A5 *Parameters for the improper dihedrals between different atom types in PBDT-TPD.*

Improper dihedral				ξ^0_{ijkl} (deg)	k^{ξ}_{ijkl} (kJ mol^{-1} rad^{-2})
SR	CW	CS	CA1	0.00000	167.4000
CW	CS	CA1	CA2	0.00000	167.4000
CS	CA1	CA2	SR	0.00000	167.4000
CA1	CA2	SR	CW	0.00000	167.4000
CA2	SR	CW	CS	0.00000	167.4000
CS	CW	CA1	HA	0.00000	167.4000
CA1	CS	CA2	CR	0.00000	167.4000
CA2	SR	CA1	CR	0.00000	167.4000
CA1	CR	CA2	CA1	0.00000	167.4000
CR	CA2	CA1	CR	0.00000	167.4000
CA2	CA1	CR	CA2	0.00000	167.4000
CR	CA1	CA2	OS	0.00000	167.4000
CA2	CR	CA1	SR	0.00000	167.4000
CA1	CR	CA2	CS	0.00000	167.4000
ST	CH	CM	CM	0.00000	167.4000
CH	CM	CM	CH	0.00000	167.4000
CM	CH	ST	CH	0.00000	167.4000
CM	CH	CM	C	0.00000	167.4000
CM	C	N	C	0.00000	167.4000
N	C	CM	CM	0.00000	167.4000
C	CM	CM	C	0.00000	167.4000
C	N	CM	O	0.00000	167.4000
CW	SR	CS	CH	0.00000	167.4000
CH	ST	CM	CW	0.00000	167.4000
N	C	C	CT	0.00000	167.4000

Table A6 *Non-bonded parameters for Coulomb and Lennard–Jones interactions in PBDT-TPD. *All hydrogen atoms in the side chains have an atom type HC, and have the same parameters presented here.*

atom type	atom name	charge (e)	σ (nm)	ϵ (kJ mol^{-1})
SR	S1	-0.0311	0.355	1.046000
	S2	-0.0561		
CW	C1	-0.0413	0.355	0.292880
	C9	-0.1090		
CS	C2	-0.0914	0.355	0.317984
	C10	0.0932		
CA1	C3	-0.1205	0.355	0.292880
	C7	-0.2428		
CA2	C4	-0.0667	0.355	0.292880
	C6	0.0145		
CR	C5	0.3021	0.355	0.292880
	C8	0.3752		
OS	O1	-0.3101	0.290	0.585760
	O2	-0.3101		
HA	HA1	0.1530	0.242	0.125520
	HA2	0.0221		
ST	SB1	-0.1638	0.355	1.046000
CH	CB1	0.2262	0.355	0.292880
	CB4	0.1508		
CM	CB2	-0.2172	0.355	0.292880
	CB3	-0.1862		
C	CB5	0.5994	0.375	0.439320
	CB6	0.5869		
N	NB1	-0.2804	0.325	0.711280
O	OB1	-0.4330	0.296	0.878640
	OB2	-0.4219		
CE	CE1	0.0895	0.355	0.276144
	CE2	-0.0600		
	CE3–CE5, CE7	-0.1200		
	CE6, CE8	-0.1800		
CT	CH1	0.0192	0.355	0.276144
	CH2–CH6	-0.1200		
	CH7	-0.1800		
HC	all*	0.0600	0.250	0.125520